NTNU

Norwegian University of
Science and Technology

Alumina Dissolution in Cryolite Melts

Formation and Behavior of Rafts

Sindre Engzelius Gylver

Chemical Engineering and Biotechnology
Submission date: June 2018
Supervisor: Kristian Etienne Einarsrud, IMA

Norwegian University of Science and Technology
Department of Materials Science and Engineering

Acknowledgment

First of all, I must thank my supervisor Associate Professor Kristian Etienne Einarsrud for his excellent advice during the semester, and always taking time for assisting me.

I will also acknowledge SINTEF for the use of their laboratory facilities and Henrik Gudrandsen for his advice and help during my experiments. Pål Ola Ulseth assisted me with the preparation and analysis of the samples, which I am very grateful of.

The project is partly funded by SFI Metal Production (Centre for Research-based Innovation, 237738). I gratefully acknowledge the financial support from the Research Council of Norway and the partners of SFI Metal Production. I will also thank all the participants of the Alumina group within this SFI for showing interest and giving advice during the semester.

I will also thank Alcoa Mosjøen, for the opportunity to do experiments at their plant during the summer 2017 and for inviting and giving me and the rest of the "alumina crew" a guided tour.

Finally, I would like to thank my friends and family for showing their support and motivating me.

S.E.G.

Abstract

Alumina is the raw-material used for aluminum production in the Hall-Héroult process. Though the process is used for several years, some phenomena is not fully investigated yet. One of those is the formation of floating agglomerates, known as rafts, when alumina is added to the cryolitic bath in the cell. An efficient feeding of alumina will reduce emissions and the energy consumption in the process.

Experiments are carried out in a lab furnace, where the goal is to create a reproducible method that investigate the formation and dissolution of rafts as a function of time, as well as changes in structure. Alumina is added into molten cryolite, and samples are pulled out at time intervals between 30 and 300 seconds. The experiments shows that at 970 °C, rafts will quickly form, and then slowly dissolve again with a constant rate of 0.8 g/min. Lowering the temperature resulted in very different results, illustrating the effect heat transfer has on the dissolution process. The effect of this should be investigated further. Pores where found in the samples, and the origin of those should be investigated, as pores will give extra buoyancy to the raft, thus increasing the flotation time.

In parallel, Computational Fluid Dynamics is used to create a model with the same dimensions as the experimental one. Simulations are done in OpenFOAM with a multiphase solver at isothermal conditions. These simulations show that air can get trapped as the alumina fall into cryolite. This can have an important effect on the structure of the raft as well as its floating ability, and should be investigated further

Sammendrag

Alumina blir brukt som råmateriale for aluminiumsproduksjon i Hall-Héroult-prosessen. Selv om prosessen har blitt brukt i mange år, er det fremdeles fenomener som ikke er fullstendig forstått. En av disse er dannelsen av flytende agglomerater, kjent som flåter, når alumina tilsettes kryolittbadet i cellen. En effektiv mating av alumina vil redusere både utslipp og energiforbruket i prosessen.

Eksperimenter har blitt gjort i en labovn, hvor målet var å lage en reproduserbar metode som kan brukes for å undersøke dannelsen og oppløsning av aluminaflåter som en funksjon av tid. Alumina tilsettes i den smeltede kryolitten, og prøver tas ut i et tidsintervall mellom 30 til 300 sekunder. Eksperimentene viser at ved 970 °C vil flåtene dannes raskt, for også løses opp sakte med en konstant hastighet på 0.8 g/min. En reduksjon i temperatur ga veldig annerledes resultater, som illustrerer effekten varmeoverføring har på oppløsningsprosessen. Effekten av dette bør undersøkes videre. Det ble funnet mange porer i prøvene, og årsaken til disse bør også undersøkes nærmere, da porer vil gi ekstra oppdrift til flåten, og dermed øke flytetiden

Samtidig har Numerisk fluiddynamikk blitt brukt for å lage en model med de samme dimensjonene som den eksperimentelle. Simuleringer ble gjort på platformen OpenFOAM med multifaseløser ved isoterme betingelser. Simuleringene viser at luft kan bli fanget mens pulveret faller ned i elektrolytten. Dette vil ha betydning for flåtens flyteevne og struktur, og bør undersøkes videre.

Contents

Acknowledgment i
Abstract iii
Sammendrag v

1 Introduction **1**
1.1 Aluminum production 1
1.2 Alumina 3
1.3 Alumina feeding 6
1.4 Objectives 7

2 Literature review **9**
2.1 Introduction 9
2.2 The behavior of alumina in the bath 10
2.3 Structure of rafts and agglomerates 14
2.4 Modeling work 21
2.5 Summary and conclusion 23

3 Cold experiments **25**
3.1 Spreading of alumina 25
3.2 Alumina in water 27
3.3 Discussion 29

4 Experimental work **31**
4.1 Background 31
4.2 Setup 31
4.3 Image analysis 36
4.4 Light microscopy 36

5 Experimental results **37**
5.1 Mass and area measurements 37
5.2 Light Microscopy 37

6 Theoretical framework **45**
6.1 Fluid mechanics 45
6.2 Multiphase flow 49

6.3 Computional Fluid Dynamics 51

7 Simulations **59**
7.1 MultiphaseInterFoam 59
7.2 Domain and mesh 62
7.3 Initial conditions 64
7.4 Boundary conditions 65
7.5 Transport properties 65
7.6 Numerical solution 65

8 Simulation results **67**

9 Discussion **73**
9.1 Mass gain and loss 73
9.2 Structure 74
9.3 Effect of changed temperature 76
9.4 Simulations 77
9.5 Industrial relevance 77

10 Concluding remarks **79**

Bibliography **85**

1. Introduction

1.1 Aluminum production

Aluminum is the most abundant metallic element in the earth's crust [10]. The metal has numerous usages, for example aircrafts, building materials and electrical conductors. It is not found in pure elemental state, and most therefore be processed. Almost all of the world's smelters produce aluminum by the Hall-Héroult process, invented in 1886 by Charles Hall in USA and Paul Héroult in France, independently of each other. In the process alumina (Al_2O_3) is dissolved into a bath mainly containing molten cryolite (Na_3AlF_6). Al_2O_3 dissolves into Al^{3+} and O^{2-} ions. By driving current through the bath, an electorchemical reactions can occur. Al^{3+} is reduced at the cathode:

$$Al^{3+} + 3\,e^- \longrightarrow Al\,(l) \tag{1.1}$$

where l is the liquid state. The anodes are located on the top of the cell and are made of carbon. This promotes a reaction where carbon is oxidized:

$$\frac{3}{2}\,O^{2-} + \frac{3}{4}\,C \longrightarrow \frac{3}{4}\,CO_2\,(g) + 3\,e^- \tag{1.2}$$

where g represent gaseous phase of state. Combining equation (1.1) and (1.2) result in the total reaction for the cell:

$$2\,Al_2O_3\,(d) + 3\,C\,(s) \longrightarrow 4\,Al\,(l) + 3\,CO_2\,(g) \tag{1.3}$$

d represents the dissolved species and s is the solid phase of state. Aluminum will have a higher density than cryolite and will therefore form a liquid phase at the bottom of the cell. Alumina and crushed frozen bath, called a crust, are added on the top of the cell in order to preserve heat and protect the anodes from oxidation in air [10]. A sketch of an aluminum electrolysis cell is shown in figure 1.1.

Production of aluminum requires large amounts of energy. An expression for the energy consumption, W_{el} is given as[32]:

$$W_{el} = \frac{U\mathcal{F}|\eta_e|}{3600 M_{Al} x_{Al} \eta_{Al}} \tag{1.4}$$

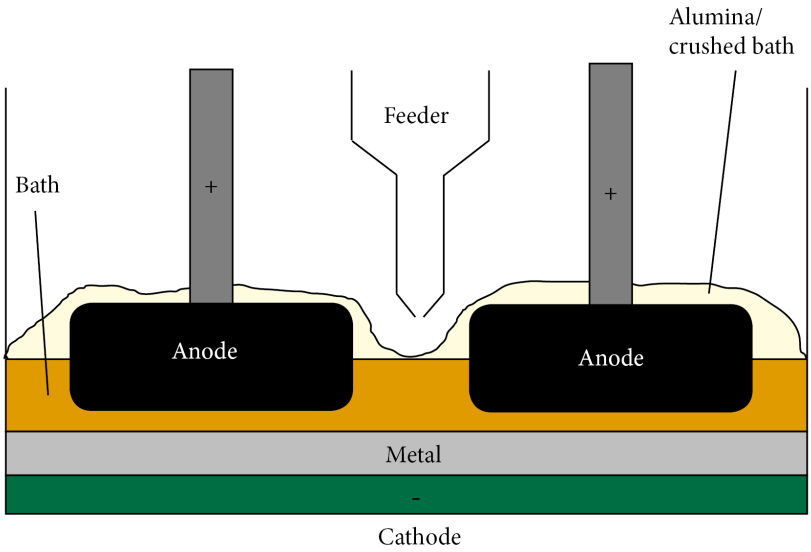

Figure 1.1: A sketch of an alumina electrolysis cell.

W_{el} is here given in kWh/kg Al. U is the applied voltage to the cell, $\mathscr{F}$ is Faraday's constant, M_{al} is the molar mass of aluminum. $|\eta_e| = 3$ and $\eta_{Al} = 1$, is the stoichiometric number of electron and aluminum, respectively. x_{Al} is the current efficiency, defined as

$$x_{Al} = \frac{i_{Al}}{i_{Al} + i_l} \tag{1.5}$$

where i_{Al} is the current density used to produce of aluminum, given by equation (1.3). i_l is the current density which is consumed by undesired side reactions. This could be due to temperature, mass transfer and other chemical reactions. Details about this are treated in Thonstad et al. [32]. Since there are only two variables, equation (1.4) can be simplified:

$$W_{el} = \frac{2.9896 \cdot U}{x_{Al}} \tag{1.6}$$

The voltage applied to the cell is normally around 4 to 4.5 V. This is much higher than the reversible voltage at 1.9 V, which is the theoretical minimum cell voltage that can be applied in order to have a reaction. Overvoltage is one of the reasons for the increase. This is due to none-ideal electrochemical behavior. Another considerable contribution is the ohmic voltage drop in the electrolyte, which can be expressed by Ohm's law:

$$U_O = RI \tag{1.7}$$

where U_O is the Ohmic voltage drop, R is the resistance and I is the current. The resistance is linearly dependent on the distance between the anode and the cathode.

Using equation (1.6) a voltage at 4.2 and a current efficiency at 90 % gives 14 kWh to produce one kg of Aluminum. Norway produce about 1 230 000 tons og aluminum [26], which requires roughly 17.22 TWh a year!

One way to increase the energy efficiency will be to reduce the distance between the anode and cathode, which gives a reduction in resistance and hence the Ohmic voltage drop explained by equation (1.7). However, this will also reduce the amount of bath in the cell. In addition, as stated by Lavoie et al. [21], modern smelters try to increase the cells' amperage for increased production. When the amperage increases, the size of the anodes must also increase, because a higher surface area is needed. Increased size of the anode without changing the size of the cells results also in lesser amounts of bath that alumina can dissolve in.

Alumina must dissolve into the bath before reaction equation (1.3) can take place. With a reduced amount of bath, an effective and fast dissolution is higher valued now than some few decades ago.

1.2 Alumina

Alumina is the raw material used for aluminum production, but is also used as a cleansing agent and as a heat preserver in the cell[31]. This section will give a overview of the alumina from bauxite until it enters the cell.

The Bayer process

Bauxite contains several minerals, among them gibbsite ($Al(OH)_3$), bohemite and diaspore ($AlOOH$), as well as oxides with other metals, for example iron. Almost all alumina is produced from Bauxite by the Bayer Process, developed by Karl J. Bayer in 1887 [14]. A flowchart of the process is shown in figure 1.2.

Since bauxite contains several other impurity oxides, one separates the aluminous minerals by extraction. Crushed bauxite is leached into a strong caustic solution at high temperature and pressure. It can be expressed by the following chemical reactions

$$Al(OH)_3 + Na^+ + OH^- \rightleftharpoons Al(OH)_4{}^- + Na^+ \tag{1.8}$$

$$AlOOH + Na^+ + OH^- + H_2O \rightleftharpoons Al(OH)_4{}^- + Na^+ \tag{1.9}$$

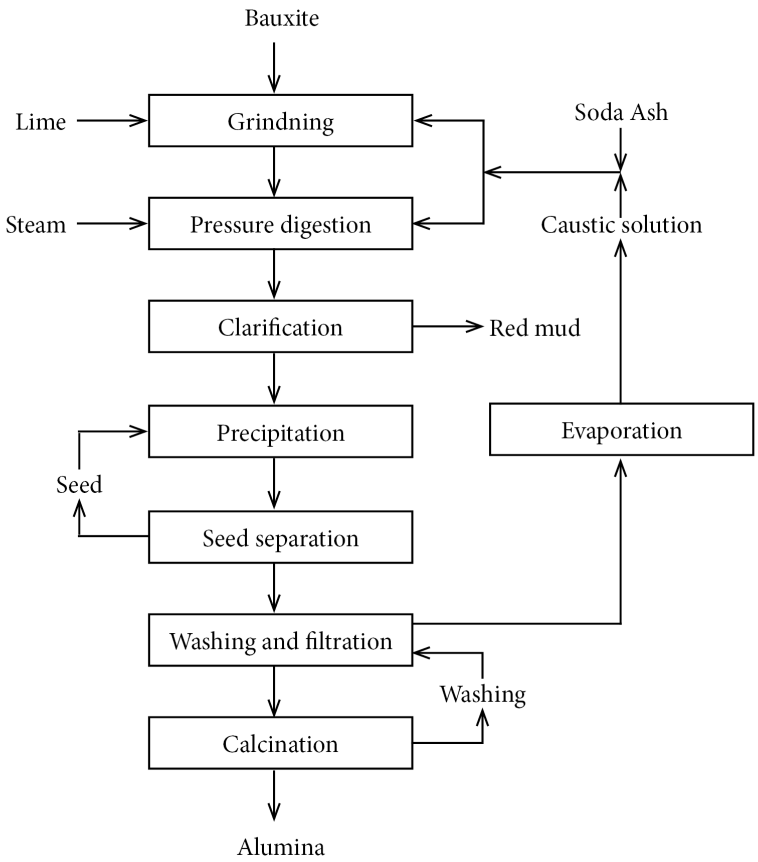

Figure 1.2: A flowchart of the Bayer process, redrawn from Grotheim and Kvande [10].

Much of the impurities will not dissolve in the solution and can be seperated in the clarification process by washing and filtration.

The sodium aluminate solution has a temperature at about 375 K when leaving the filters. It must be cooled down in order to precipitate. Seeds of $Al(OH)_3$ are present in the solution for increasing the precipitation speed. Solution and seeds are driven to continuous tanks, and some seeds are recycled back while the rest is transported further on.

The final stage is calcination. Gibbsite is converted into various crystallographic forms of alumina in a rotary klin or fluid bed calciner. Different pathways are shown in figure 1.3. Most of the Gibisite is believed to follow pathway (b). α-alumina is the stable phase, while the other are metastable phases.

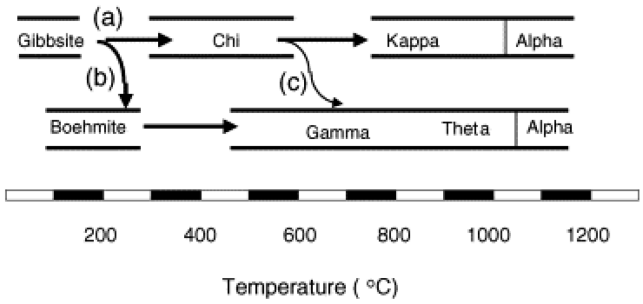

Figure 1.3: Different pathways for calcination of alumina, by Whittington and Ilievski [41]. For the Bayer process, pathway b) the path most of the Gibbsite goes through when calcinated.

It is desired to remove as much moisture at possible, but at the same time avoid a large amount of α-alumina in the final product, as it has negative effects on the dissolution[14]. The final powder is therefore particles made up of polycrystalline and polymorphic aluminum oxide.

Dry Scrubbing

In most modern smelters, alumina will go through a dry scrubbing process before it enters the cell. Alumina will acts as a sorbent of fluoride gases that are emitted from the cell. This is beneficial for the environment and will also recycle some expensive fluorides back to the cells [10]. Alumina that has gone through the process is called secondary alumina or Smelter Grade Alumina (SGA). In addition, secondary alumina will also dissolve faster than the primary, making dry scrubbing even more beneficial [44].

1.3 Alumina feeding

The feeding of alumina is done by point feeders. An illustration of a point feeder is shown in figure 1.4. A breaker hits the crust before and alumina is then fed into the bath. Between 0.5 and 2 kg alumina is added each time, with time interval varying between 1 and 3 minutes. An alumina concentration around 2 to 4 mass% is required for an effective process [10]. A too low concentration will give anode effects, causing high cell voltages and emissions of hazardous fluorocarbons. A too high concentration will result in undissolved alumina, creating operational disturbances[21].

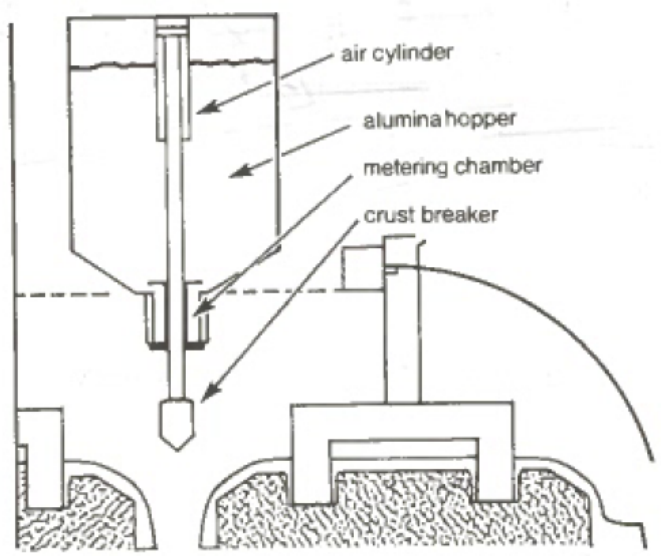

Figure 1.4: Illustration of a modern point feeder, from Grotheim and Kvande [10].

Alumina feeding in the cell is a complex process. Since alumina will enter the bath with a temperature at about 100 °C, a large amount of heat is required for alumina to reach the temperature of the bath [32], making heat transfer important. Interactions between different particles and phases, as well as mass transport of alumina in the cell due to flow in the bath and diffusion must also be considered. However, the mechanisms of the alumina dissolution is not throughly investigated, and more work is needed to fully understand the dissolution process.

1.4 Objectives

The focus on this thesis will be on the formation on floating rafts which occur during feeding. For obtaining more knowledge, two alternatives are investigated for this thesis: Laboratory experiments and simulations.

Laboratory experiments are done for gaining more knowledge about interactions between alumina and bath as a function of time. The advantage of using a laboratory furnace instead of industrial cell is that one has better control on variables. Developing a reproducible method will create a opportunity to compare measurements where different parameters(for example temperature and alumina properties) are varied. Overall objectives can be summarized as:

- Develop a reproducible method that can be used to create and fetch floating rafts in a laboratory cell.
- Investigate variation of mass and composition of layers for rafts as a function of time.
- Investigate how a difference in bath temperature affects the raft formation.

The interior of an aluminum electrolysis cell is a harsh environment, where it is hard to make any observation and recordings on both industrial and laboratory scale. Simulations can therefore give information about phenomena that cannot be observed, provided that the model is good. Objectives for the simulation work during this thesis can be summarized to be:

- Create an isothermal Volume of fluid (VOF) model with the same dimensions as the laboratory cell.
- Observe if simulations can give an explanation of phenomena found in laboratory samples.

Chapter 2 will give more details about alumina dissolution and formation raft, as well as a review of earlier research done within this field. Chapter 3 contains description of setup, results and discussion of cold experiments done as a preparation for the laboratory experiments. Detailed setup and descriptions of the experiments are given in chapter 4, with results in the following chapter. Chapter 6 will give an introduction to the theoretical foundation for the simulations. Detailed descriptions about the simulations are given in chapter 7, with results following in chapter 8. Finally, a discussion is given in chapter 9 before concluding remarks in chapter 10.

2. Literature review

2.1 Introduction

Dissolution of alumina in cryolite has been studied for many decades. Alumina can be dissolved in two ways: as dispersed grains, or as agglomerates. Several researches have measured the dissolved alumina as a function of time [33][18][12][29]. One curve from the work of Haverkamp and Welch [12] is shown in figure 2.1. In the first part, well dispersed alumina will dissolve immediately. Some alumina will form lumps known as agglomerates or rafts. They will dissolve more slowly as shown in the right part of figure 2.1.

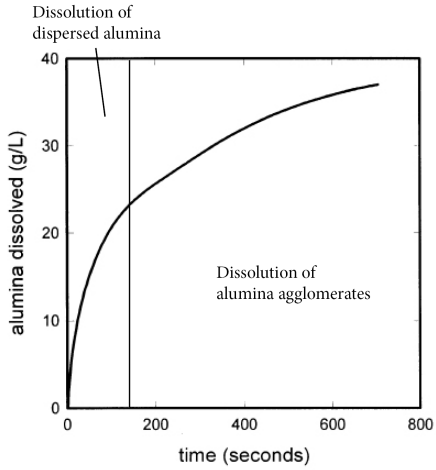

Figure 2.1: A dissolution curve from Haverkamp and Welch [12].

Lavoie et al. [21] suggest a four step process for the dissolution, illustrated in figure 2.2. In the first step is the rapid dissolution explained earlier, while the slow dissolution can be divided into three more steps. Due to temperature differences, bath will freeze around the particle surface. Particles close to each other freeze into larger platelets, known as agglomerates. The frozen bath must be remelted before further dissolution can occur. Agglomerates might be partly surrounded by bath, creating a floating raft on the surface of the bath, where alumina powder will be located on the top of the raft. Bath can also freeze fully around the alumina. The density of these agglomerates can

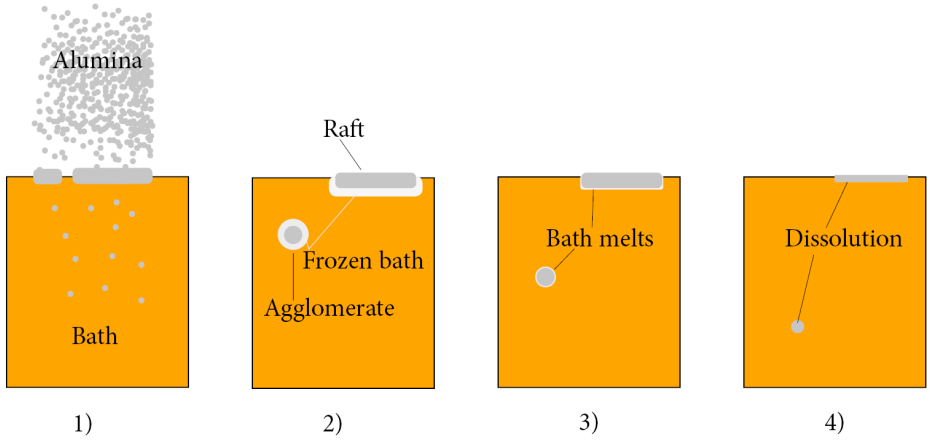

Figure 2.2: Illustration of the four step process as described by Lavoie et al. [21]. 1) Alumina hits the bath. Well dispersed alumina will dissolve immediately. 2) Bath will freeze around the particle, creating a raft. If bath manage to cover all alumina, a spherical agglomerate are created, which might sink. 3) The frozen bath must remelt before further dissolution. This step is heat transfer controlled 4) After the layer has molten, dissolution can continue. If there is a lack of available heat, steps 2)-3) might then be repeated.

be higher than the density of the bath and molten aluminum, and the agglomerates will then sink to the bottom of the cell, creating sludge [37][39]. Since the dissolution reaction is endothermic [40], the last steps might be repeated several times before the batch is completely dissolved.

Sludge should avoided as it will disrupt the current paths in the cell, lowers the current efficiency and will give a fluctuation of alumina content, resulting in operational disturbances [19].

2.2 The behavior of alumina in the bath

Agglomerates can both float and sink. Three forces will act on a particle floating on a liquid. Firstly, the gravitational force, F_g

$$F_g = V_p \cdot \rho_p \cdot g \tag{2.1}$$

V_p and ρ_p are the volume and density of the particle, respectively, and g is the gravitational acceleration.

The buoyancy force, F_b, can be expressed as

$$F_b = V_i \cdot \rho_l \cdot g \tag{2.2}$$

V_i is the immersed volume of the particle and ρ_l is the density of the liquid. Finally, interactions on the surface will be a source to forces, expressed as:

$$F_s = l \cdot \gamma \cdot cos(\delta) \tag{2.3}$$

l is the triple line, γ is the surface tension while δ is the contact angle. A particle will float on the surface as long as the sum of the forces equals zero. Calculations from Kaszás et al. [15] point out that the contact angle, which affects wetting of the powder, is an important parameter for flotation, but also very difficult to measure. They also pointed out the angle of repose, bulk density and Braunauer, Emmet and Teller (B.E.T) specific surface area as important parameters.

Other alumina properties will also affect the dissolution. Lavoie et al. [21] points out the particle size and content of α-alumina as important properties affecting the dissolution. Moisture, often measured as Loss On Ignition (L.O.I) is also found to be an important parameter [10]. Details about these properties can be read in Grotheim and Kvande [10]

The importance of the surface tension for flotation was pointed out in a later study by Kaszás et al. [17]. 12.5 mL SGA was compressed into discs with 40 mm diameter and 8.6 mm thickness. These discs were added on a free surface of bath in a $7.6 \cdot 7.6$ cm square crucible with a bath height on 3.8 cm. The discs were removed after a certain time in the bath. After the discs were removed, they were weighted and the density of the raft were estimated. A plot of the density as a function of time is given in figure 2.3. As the density of the raft exceed the bath's density, it can be concluded with that the surface tension plays an important role in keeping the rafts floating.

Kaszás et al. [16] have also done recordings of alumina being fed to cryolite. A $7.6 \cdot 7.6$ cm crucible was filled with cryolite, such that the bath height was 5 cm. Batches of alumina powder, with mass varying between 0.1 to 2 grams were fed to the bath through a steel tube. A video camera mounted above the bath recorded the behavior after feeding. Image processing in Matlab was used to estimate the thickness, angle of conical and radius of curvature of the rafts. The infiltration and the areas of the rafts were also measured. They found out that the superheat played an important role. With increasing superheat, the disintegration happened faster and spreading of the raft was larger. Their work shows the possibilities how modern image processing can increase the understanding of the process.

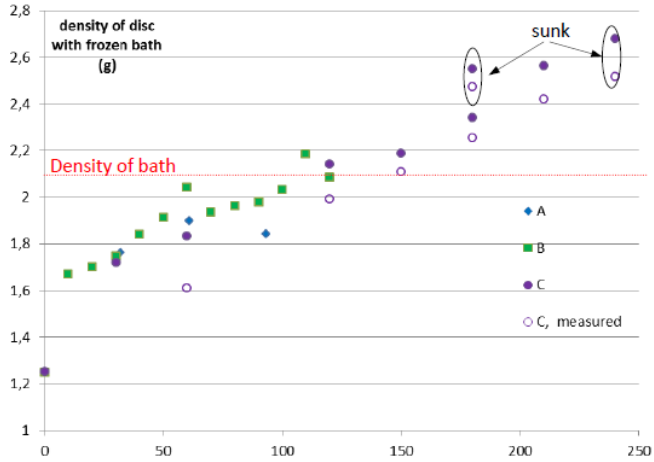

Figure 2.3: Plot of density of alumina discs as a function of flotation time by Kaszás et al. [15].

Walker [38] observed the feeding of in an industrial cell and observed a coherent floating island, which unlike the hard crust has a highly viscous and mushy consistency. In his experiments, 8 kg alumina was fed into a bath surface about $0.2 \cdot 1.5$ meters.

Formation of rafts in industrial cells has also been recorded by Gylver [11]. The crust was broken in order to get a better view of the bath surface. Images from one of the recordings are shown in figure 2.4. The flotation time and behavior varied for different cells.

Other techniques has been used to visualize the addition of alumina. Walker et al. [37] used an x-ray furnace to visualize the alumina feeding. It was shown that the alumina will penetrate and sink into the bath. A frozen shell was created around, and the newly created agglomerate then floated up to the surface. After a while, the agglomerate starts to sink down into the bath again. According to the authors, this is due to infiltration of bath into the alumina after the outer frozen layer has melted. This will increase the density of the agglomerate and force it to sink.

See-through cells have been used by several researchers. A see through cell contains sidewalls with quartz glass windows, which makes it possible to observe the bath from the side. Liu et al. [22] compared addition of α- and γ-alumina, and found out that α-alumina tends to sink to the bottom of the cell, while γ-alumina floats and sinks down slower in form of agglomerates. Yang et al. [44] compare addition of primary and secondary alumina, and conclude that secondary alumina dissolve better as smaller

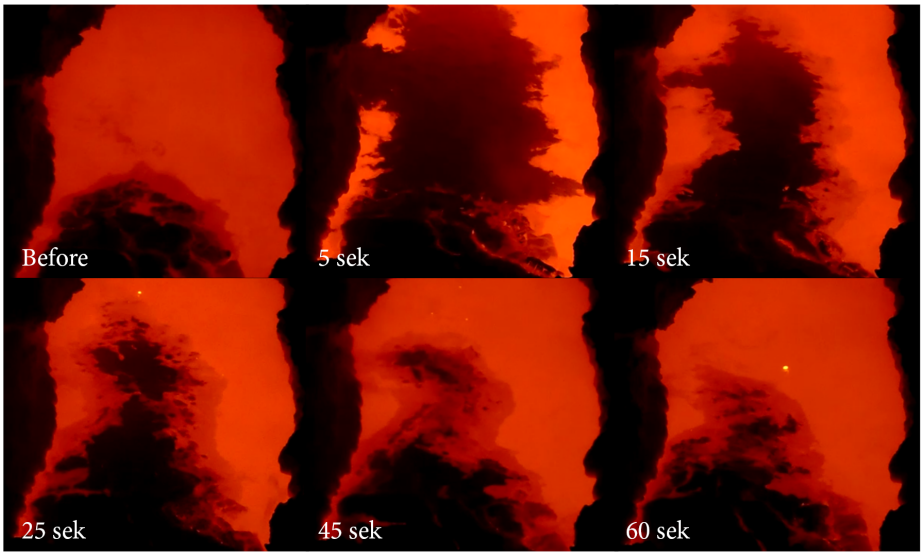

Figure 2.4: Recordings of a batch of alumina added to an industrial cell in Alcoa Mosjøen[11]. The time is set relative to the time of feeding.

agglomerates are formed, resulting in a higher surface area per volume alumina added. Another study[42] by the same authors investigate the dissolution rate of alumina with different properties and varying bath chemistry.

The same experimental procedure has been done to investigate the dissolution of rafts formed from SGA as well[43]. A scale is rigged within the cell. 5 grams of alumina where then added to the cell, after an agglomerate was formed on the top of the bath, it was immersed into the bath, and the weight of the crust as a function of time could be measured. They found that no mass was reduced at the start due to heating of the crust, followed by a linear reduction. This can be seen in figure 2.5. They also investigated the dissolution rate at two different temperatures. It was concluded that increased superheat increased the dissolution rate. The dissolution rate was in order of 1 g/min.

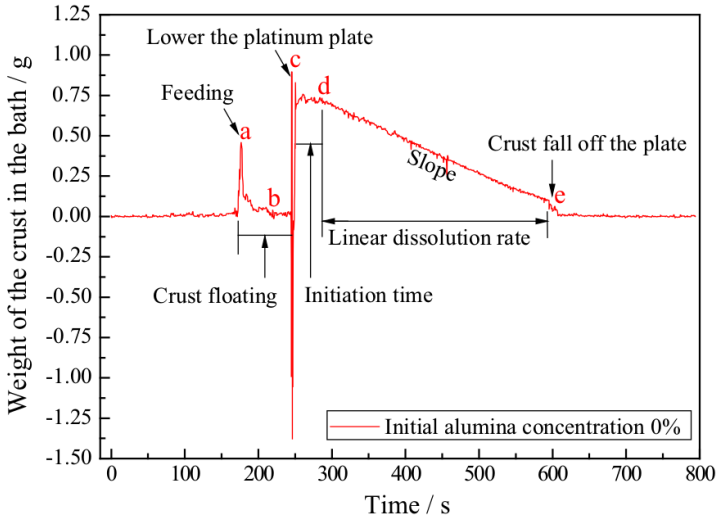

Figure 2.5: Plot of weight of the crust as a function of time by Yang et al. [43]. A crust formed by adding alumina to the bath is formed, and lowered down in the bath at point c.

2.3 Structure of rafts and agglomerates

The formation of raft and agglomerates has mainly been investigated in lab scale. One assumes that the freezing of bath around the agglomerates has a similar mechanism as the freezing of crust. The structure is dependent of two reactions: The rapid heating of alumina as it enters the hot bath and the rapid freezing of bath as it is exposed to cold alumina.

When heated, γ-alumina will transform rapidly into α-alumina as shown in figure 1.3. The α-crystals that form tend to create platelets and form an interlocking matrix [34]. This gives a strong structure, which is due to sintering. Sintering occurs when a powder is exposed to high temperature and a mechanism for material transport is present. Particles will start to rearrange and neck formation will occur at points where particles are connected together. An analogy is the melting and freezing of snowcrystals into a more compact ice layer. The necking and rearrangement will result in a decrease in porosity, creating a compact layer. Details of sintering mechanism in general are described by Richerson [28] and the dissertation by Østbø [31] also contain a good description related to alumina sintering.

Walker et al. [39] created cylindrical agglomerates by packing powder of both α- and γ-alumina in aluminum foil and immersing them into the bath in an industrial cell. A photograph of the cross-section of one the cylindrical agglomerates is shown in figure 2.6. It shows that the a agglomerate contains several layers, which are can be easily separated from each other. The same structure has also been found by other researches[31]. The outmost layer is frozen bath, while the two infiltration layers could be called a sintered layer.

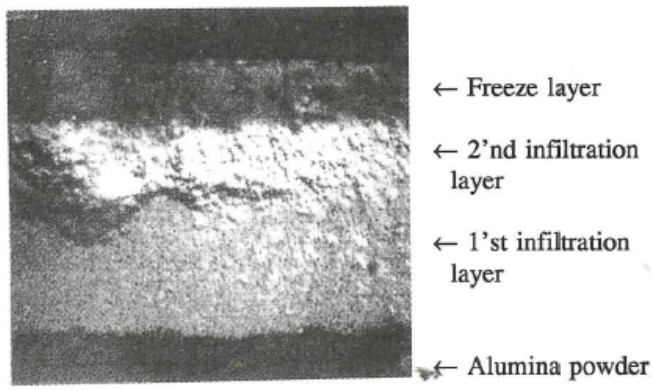

Figure 2.6: Photograph of cross-section cylindrical agglomerate obtained by Walker et al. [39].

In order to understand the freezing of the bath, one can consider the NaF-AlF_3 binary phase diagram. A part of the phase diagram is given in figure 2.7. Pure cryolite, Na_3AlF_6 is in the left part of the diagram, and melts congruently at 1010 °C. This is indicated by point 1) in the figure. Smelters will have an AlF_3-concentration above the concentration of cryolite in order to lower the liquidus temperature, resulting in lower operating temperature. This is often expressed as excess wt% AlF_3 or bath acidity. Normal range for most smelter is in the range between 8 to 12 wt%.

Figure 2.7 marks the composition of the different layers in the agglomerates created by Walker [38], calculated by X-ray diffraction (XRD). 2) is the composition of the outer freeze layer, 3) the first infiltration layer and 4) the second infiltration layer. The different composition of the layers will give an indication on how fast the bath will freeze. Immediately freezing, also known as quenching, will give a composition close to the actual composition of the liquid bath. This indicates that the outmost frozen layer is the result of rapid freezing as cold alumina hits the bath. In a rapid cooling process, ions will not have time to escape from solid phase before it is trapped. The reheating of the layer will go more slowly, and the the phase diagram is then more applicable.

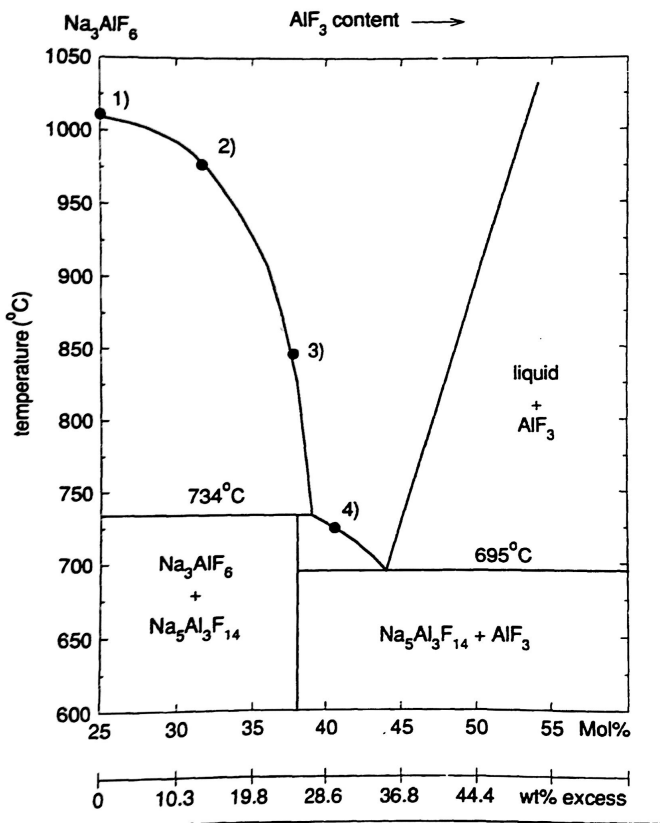

Figure 2.7: Part of the binary phase diagram NaF-AlF_3 from Walker [38].

At about 695 °C, chiolite, together with aluminum fluoride, will melt in an eutectic reaction.

$$Na_5Al_3F_{14} + AlF_3 \longrightarrow \text{liquid} \tag{2.4}$$

creating an AlF_3-rich liquid, which infiltrates into alumina. It will freeze with a composition given at point 4). Another infiltration will occur at about 850 °C, with composition indicated by point 3). As the temperature of the agglomerate increases, the frozen layer will melt and the infiltration will go deeper into the agglomerate. This will fill up voids in the agglomerate and increase the density, which in turn will result in sinking.

It should be noted that the points drawn in the phase diagram in figure 2.7 might not reflect the actually chemical composition, as the points are found by detecting the liquidus of the layers. The phase diagram assume a pure NaF-AlF_3 solution, while an industrial bath will contain noticeable amounts of Al_2O_3, CaF_2, MgF_2 and LiF, which will lower the liquidus of the melt.

The variation within an industrial raft is visualized in a study by Dando et al. [3], where SGA was added to an industrial cell and rafts were formed. The rafts were skimmed out, and Scanning Electron Microscopy (SEM) was preformed on different parts of the rafts. It showed that alumina in the upper part of the raft has not gone through a phase-formation yet, and was not fully infiltrated by bath. Further below, alumina undergoes a transformation into platelets. At the bottom, alumina has been transformed into eutectic phases in a matrix of bath. SEM images from different cross sections are shown in figure 2.8. This supports the theory that the platelet transformation is important for agglomerate formation.

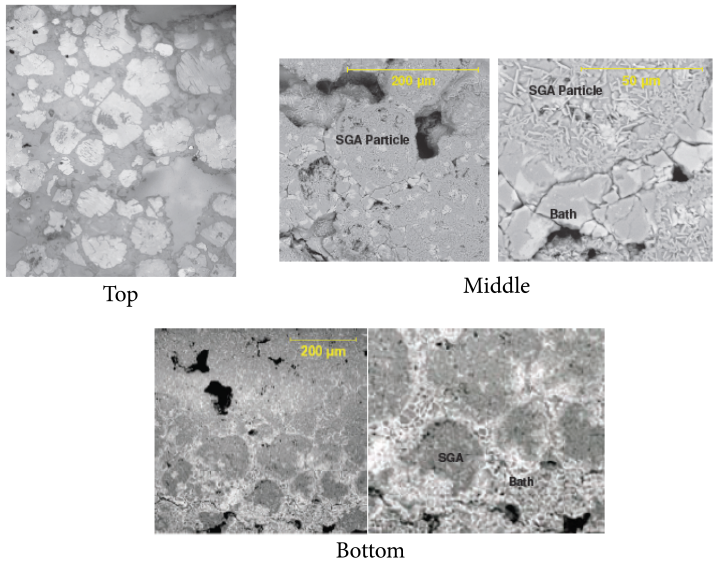

Figure 2.8: SEM image for a cross sections of a raft done by Dando et al. [3]. Rafts were created by adding SGA to a industrial cell. The top section was on the top of the raft. The middle cross section was close to the bath surface upon removal from the cell, while the bottom was below the bath surface.

Gylver [11] has also obtained rafts from industrial cells as a part of his project work. Computed Tomography (CT) images of vertical cross sections from two industrial rafts are shown in figure 2.9. He shows that there are large variation within a raft, as well as between different rafts. CT-images has also been done by Picard et al. [27], with frozen bath samples from the anodes. They also found significant differences in porosity within the sample, where the most porous part was the part of the sample with the longest distance from the anode, i.e the longest distance from the bath being rapidly frozen.

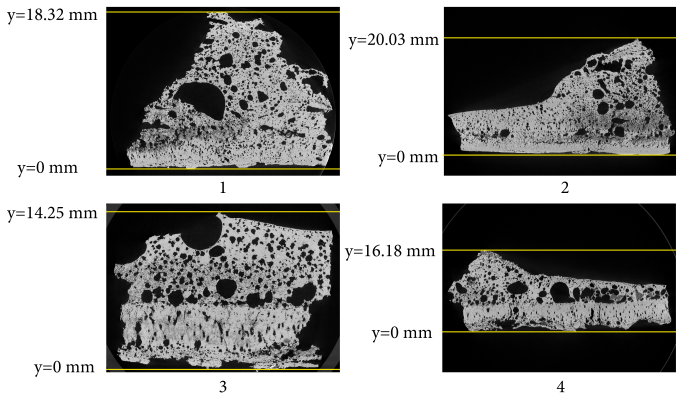

Figure 2.9: CT-images of the cross section for four different rafts, obtained by Gylver [11]. Image 1 and 2 are from the same sample. Image 3 and 4 are also from the same sample.

In research done by Rolseth and Thonstad [29], both primary and secondary alumina were added to a laboratory cell containing bath saturated by alumina with a superheat at about 20 °C. Since a large of amount of alumina was added, a crust was created, and this was collected immediately. Vertical sections of the crusts are shown in figure 2.10. They also collected floating rafts from an industrial cell during anode changing. The agglomerates form had a similar appearance as the ones obtained at the lab. Agglomerates from secondary alumina seemed to have a more porous and gray structure than the primary one. Possible sources of the pores is however not commented in the paper.

Yang et al. [43] commented the porosity in their study. They had a platinum plate located in the bath connected to a scale. They could then measure the weight of the crust as it was dissolved in the bath. In addition, several samples were withdrawn from the bath. Alumina content was found by dissolving the crust in aluminum chloride. The measured density was found to be lower than the calculated one if assuming that the agglomerate only contains bath and alumina. They believed that this is due to pores formed inside the crust. The porosity was calculated to be in the range of 6-8 %. The origin of the pores was discussed to be rapid release of structural hydroxyl and absorbed moisture.

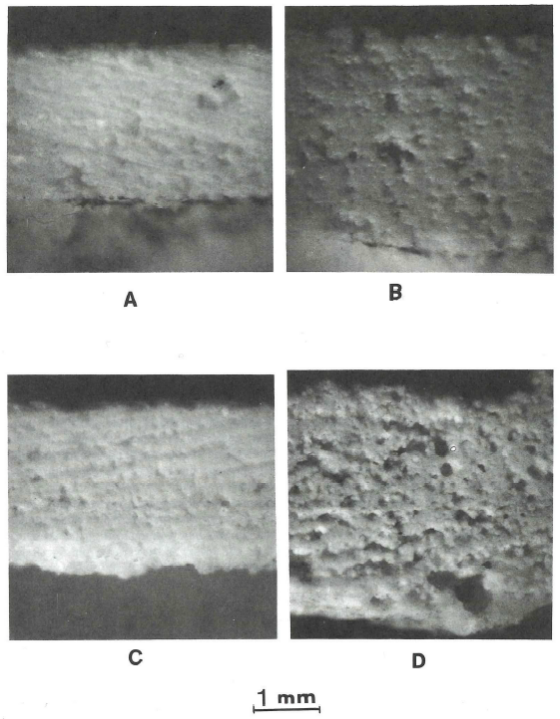

Figure 2.10: Vertical sections from samples of crust collected immediately after addition of alumina by Rolseth and Thonstad [29]. A and C are primary alumina from two different suppliers. B and C are secondary alumina, where B and D is from the same supplier as A and C, respectively.

Walker et al. [39] did industrial measurements of agglomerates by immersing an steel mesh basket into the bath of a cell, under a feeder. The basket was withdrawn from the electrolyte with varying time. The basket contained frozen electrolyte, together with many agglomerates formed as ellipsoids, which he called subislands. These agglomerates was 1-2 cm high and 1-5 cm in diameter. Since the measured density of the agglomerates increases to values above the density of aluminum, it indicates that there are agglomerates fetched would have sunken to the bottom of the cell if not for the basket present.

Kobbeltvedt [18] has done experiments where at most 140 g alumina were added into unstirred cryolite in a round crucible with an inner diameter of 20 cm. Agglomerates were retrieved by a sieve that was already immersed in the bath. Superheat, flotation time and batch size were varied. Thickness of rafts was measured after fetching, found to be in range between 5 to 15 mm. The thickness varied within the sample, but it was found that increased superheat and longer flotation time gave a smaller thickness. A

reduced batch size did not change the thickness, due to its spreading over the surface was smaller. The underside of agglomerates at a superheat of 10 °C were very porous, while agglomerates obtained at superheat of 50 °C did not have pores. This was explained with that the porous layer melt away first. The origin of the pores was however not discussed.

In another work by Walker et al. [37], artificial agglomerates was created by packing alumina into aluminium foil and immersing it into a bath of cryolite in a laboratory furnace. The temperature of the powder as a function of time was measured using a thermocouple. In addition, alumina was pulled out at varying time, and the size of the frozen layer as well as the weight of the created agglomerates was measured. This is also shown in figure 2.11. They found also out that the frozen layer decreased with increasing temperature, AlF_3-content, and stirring power.

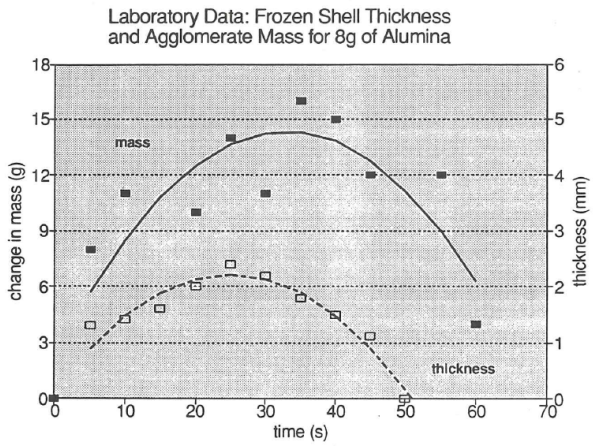

Figure 2.11: The mass change and thickness of frozen layer of artificial agglomerates as a function of time, by Walker et al. [37].

The same experimental setup was adopted by Kobbeltvedt [18] and Østbø [31] in their dissertations. Kobbeltvedt [18] measured the temperature at the different locations in the agglomerate. His most important finding is that the heat transfer of the agglomerate is slow enough to allow formation of an interlinked network of alumina grains. He also showed that pure α-alumina will not create such a network.

Østbø [31] had his focus was to study the agglomeration on a micro-structural level. His research will not be discussed in detail here, as the micro-structure of the agglomerates is beyond the scope of this thesis.

2.4 Modeling work

As the quality of alumina, chemical composition of the bath and temperature of the cells will vary, a model that can predict the dissolution of alumina would be valued. A model would also be an useful to supplement laboratory measurements. It can also be used to explain phenomena that cannot be seen in a laboratory cell.

A model must handle the interactions between the alumina particles and free surfaces. Secondly, the condition of the free surface must be realistic to the surface in an electrolysis cell. Finally, a model must consider chemical reactions that occur and heat transfer, in particular the freezing and melting of the alumina rafts and agglomerates.

This section will focus on the dissolution of agglomerates and rafts.

Dassylva-Raymond et al. [4] create a model by dividing the the dissolution int to five phenomena: moisture evolution, solidification/melting with mass diffusion, liquid and gas infiltration, the alumina sintering and finally the dissolution itself. Their results were compared with the experimental results by Walker [38], also shown in figure 2.11. The model estimated correctly the lifetime and frozen layer thickness, but its shape of the curve was not the same as Walker's. Details of how the different steps were modeled will not be treated here, but it gives a good overview for steps that should be considered further.

Zhan et al. [45] use Computational Fluid Dynamics (CFD) to create a heat- and mass transfer model to investigate the dissolution of both dispersed alumina and agglomerates. They found that agglomerates with diameters from 4 mm and higher dissolved in order of 100 s. Increased bath superheat and higher temperature of the alumina added also gave an increase in dissolution rate.

CFD has also been done by Einarsrud et al. [7], where the drop of alumina from the feeder and into the bath was investigated. For simplicity, the alumina was assumed to be a rigid particle. Density and drop height of the particle was varied in order to see how this parameters affected the feeding. A summary of the most important results are given in figure 2.12. The work illustrates that there will be complex interactions between dose and liquid. Figure 2.12b) shows that the particle will entrain a lot of bath when emerging from the bath surface, creating an opportunity for bath to cover the whole or parts of the raft surface. This model does however not consider spreading of the dose, which will happen quite fast after the dose hits the bath.

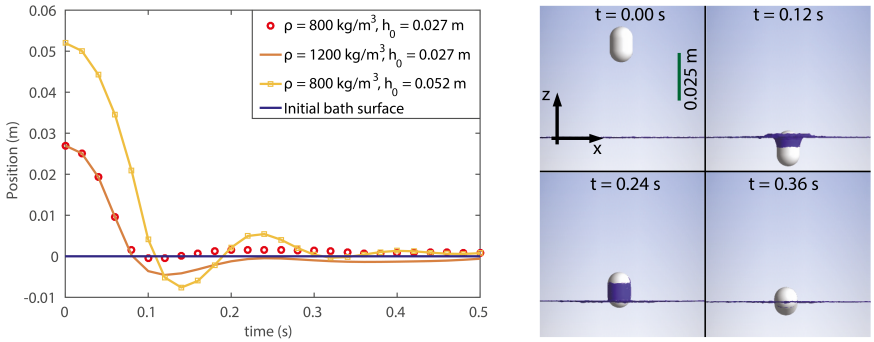

Figure 2.12: Overview of the must important results from the simulations of [7]. a) Shows the position of dose center of mass, for three different cases, where density ρ and drop height h_0 is varied. The bath surface is located at position = 0. b)Shows the motion of a particle with density 800 kg/m^3 and drop height 0.052 m.

Further investigation was done by Gylver [11] in a 2D model, where the alumina dose was assumed to be a liquid. Drop height, density, viscosity and surface tension were varied. One illustration is shown in figure 2.13. As the shown in the figure, an unwanted contraction happens due to the surface tension. Another interesting finding is that some small bubbles of air is observed underneath the floating "raft". This might explain the origin of some of the pores found in the industrial sample.

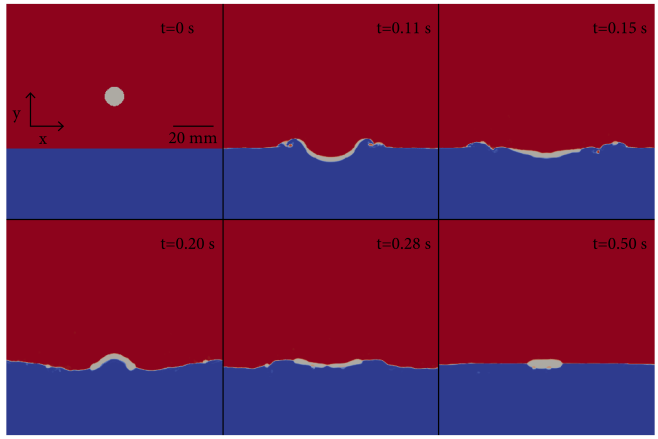

Figure 2.13: Motion of dose with drop height 0.054 m, density 1200 kg/m^3 kinematic viscosity 10^{-6} m^2/s and surface tension 0.07 N/m.

2.5 Summary and conclusion

Although a lot of work has been done through the last decades, the formation of rafts and agglomerates is not fully understood yet. There is lack of description of rafts from industrial cells. Most studies focus on the whole dissolution process and dissolution of artificial agglomerates. Significant work was done in the 1990es by Kobbeltvedt [18], Østbø [31] and Walker [37]-[39]. Walker's dissertation [38] is the most relevant, with description of industrial agglomerates, and studies of agglomeration as a function of time and the effect of temperature, bath acidity and stirring has on the formation and disintegration of the agglomerates.

Kaszás et al. [15]-[17] has done a lot of work over the last years, and shows the opportunities modern recording and image analysis can increase the understanding of raft formation. A see-through can also give a lot of interesting observations on the phenomena that cannot be seen from the bath surface [42]-[44].

Modeling related to alumina dissolution is mostly done for alumina that already has entered the bath, and does therefore not consider the transport of alumina from feeder to bath. A model must consider both heat and mass transfer, as well as coupled interactions between particles. Dassylva-Raymond et al. [4] point out important phenomena to consider when creating a model. Einarsrud et al. [7] demonstrate the first step of feeding and illustrate complex interactions that might occur.

The review shows that there has been few experiments about alumina raft formation. Research has been done on artificial agglomerates, such agglomerates does not consider the interactions that will occur as the alumina powder is fed down into the bath. More experiments at laboratory is needed in order to gain better insight about the mechanisms of the formation and disintegration of rafts. An advantage with laboratory scale experiments, is that parameters can be controlled easier than in an industrial cell, and it can be compared with both other experimental and modeled results.

3. Cold experiments

The Hall-Héroult process is carried out at high temperature in a hazardous and aggressive bath. Since it is hard to observe and record, some cold experiments were carried out in order to get a better knowledge of what is happening when alumina is added to the laboratory cell.

There is a height about 50 cm between where bath can be fed and the bath surface. It is therefore important to find a suitable way to deliver alumina into the cell, preferably as similar as an industrial feeding. Experiments should therefore be carried out in order to find out how feeding of alumina should be done in the laboratory cell.

3.1 Spreading of alumina

The motivation for this experiments was to see how the drop height affected the spreading of alumina. If alumina is added in such a way that it will be dispersed when entering the bath, no rafts will be formed.

Experimental setup

A 50 cm long pipe with a inner diameter of 1 cm was placed over a paper. A sketch is shown in figure 3.1. The height between the paper and the end of the pipe was varied. Alumina was released from both the top and the end of the pipe. Parameters for the different setups are given in table 3.1.

Table 3.1: Overview of experiments for spreading of alumina.

Experiment #	Released from	Total drop height	Amount Alumina
1	top of pipe	54 cm	2 g
2	top of pipe	51 cm	2 g
3	top of pipe	60 cm	2 g
4	bottom of pipe	10 cm	2 g
5	bottom of pipe	1 cm	2 g

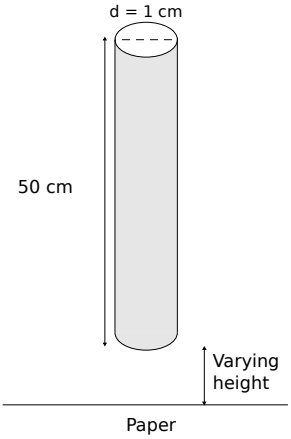

Figure 3.1: Sketch of the setup.

Results

Images from the different test are shown in figure 3.2. Higher drop height gave a bigger spreading. However, video recording showed that spreading happens as alumina hits the paper.

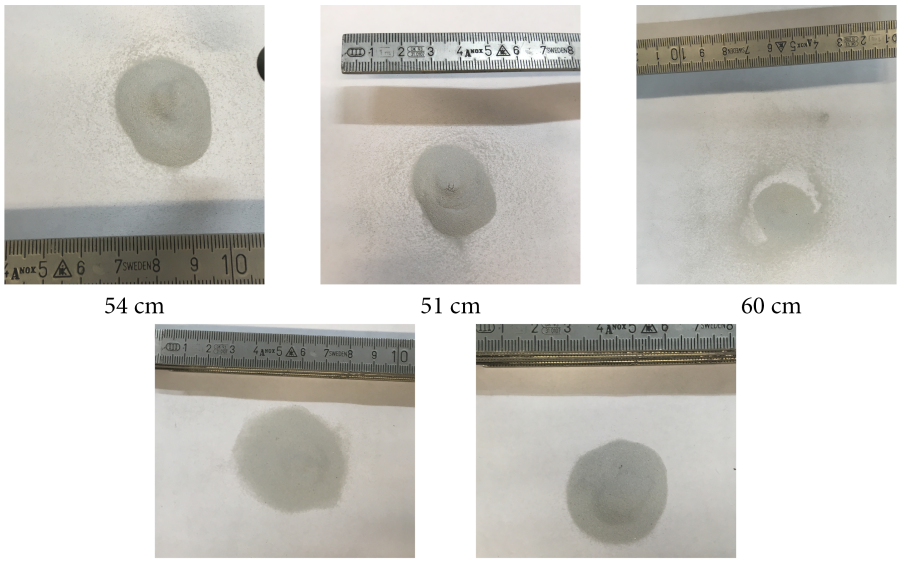

Figure 3.2: Images of 2 gram of alumina dropped from different heights.

3.2 Alumina in water

Finding a liquid at room temperature with same properties as cryolite bath is challenging, as the surface tension, density and viscosity are very high. The background for this experiments was to get an indication of what will happen when alumina is added to a liquid. The goal is to see if there is any height or feeding method, which is preferred in the laboratory experiment. It will also be possible to see if there will be any splashing when alumina is added. Splashing is an unfortunate effect as cryolite is a very hazardous liquid, which can create damages on equipments.

Clean water and saline solution was chosen as liquids. As shown in table 3.2, surface tension and density are lower than for an industrial cell cell. However, experiments could give some insight in for example how the surface tension and density affect how alumina float.

Table 3.2: Physical data for water, a saline solution and cryolite.

Liquid	Surface tension [mN/m]	Density [kg/m^3]	Viscosity [mm^2/s]	Reference
Water	72.8	998.8	1.003	[30]
Water with 15 wt% salt	77.9	1108.5	1.215	[30]
Cryolite	140	2100	1.30	[5]

Experimental setup

A glass beaker with a diameter of 10 cm was filled with a water, approximately to a height of 10 cm. The saline solution was made by adding 90 grams of NaCl into 600 gram water. 1 gram alumina was added from different heights, as shown in table 3.3. A Sony Camera was used to record the feeding. The frame rate was 500 fps

Table 3.3: Overview of experiments for alumina added into water.

Run #	liquid	Released from	Total drop height	Amount Alumina
1	water	top of pipe	54 cm	1 g
2	water	bottom of pipe	4 cm	1 g
3	water	bottom of pipe	1 cm	1 g
4	water	top of pipe of pipe	60 cm	1 g
5	water	bottom of pipe	3 cm	1 g
6	saline solution	bottom of pipe	3 cm	1 g
7	saline solution	top of pipe	53 cm	1 g

Results

Screenshots from run 5 and 7 are shown in figure 3.3 and 3.4, respectively. In all the runs, alumina penetrated the water and sank down to the bottom of the beaker. Some particles tended to stay afloat when the total drop height was high, and the more particles floated in the saline solution. It is also observed bubbles of air that elapse from the powder as it sinks to the bottom. These are indicated in figure 3.3, but are too small to be seen properly in figure 3.4.

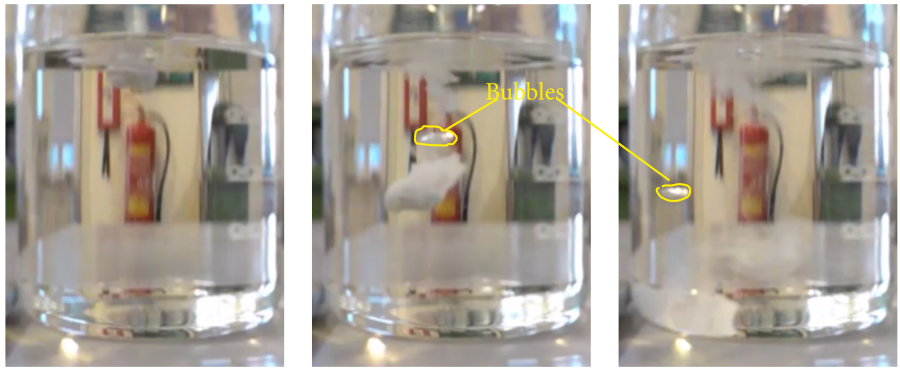

Figure 3.3: Images of alumina fed in water from a total drop height of 3 cm.

Figure 3.4: Images of alumina fed in a saline solution from a total drop height of 53 cm. Bubbles were observed, but are not visible in the current images.

3.3 Discussion

The background for these experiments was to see if it is possible to predict how the alumina will behave as it is added to cryolite.

The first experiment show that an increased height between pipe and surface gives a bigger spreading. Increasing drop height will gives increased velocity for the particles when they hit the surface. The particles will then hit the surface with a larger force, resulting in larger spreading. Although cryolite is a liquid, the same effect could be observed due to its high surface tension and density. Alumina should therefore be released as close as possible to the bath surface. This will avoid dispersion of particles.

Feeding alumina from the top of the pipe gave a more continuous feeding than dropping from the bottom of the pipe. This is due to different feeding techniques. Alumina should be fed as a batch in order to avoid dispersed particles, as the task for the experiment is to form agglomerates. A batch is also preferred since it is the same way as feeding are done in the industry. Having a pipe with a lid that can be opened will secure that the alumina is hits the bath as a batch and also give a lower drop height and hence velocity for the powder.

The release of gas is also an interesting phenomenon. As discussed in earlier work[11], a reason for pores in raft could be trapped air. Recordings shows that the air is trapped as alumina is fed into the bath and then released as the batch sinks down. In a real case, bath will probably freeze around alumina so fast that the trapped air will not be released from the agglomerate. Splashing was not observed in the experiments, and it should hence be possible to use the same technique in a furnace.

Alumina particles dropped from the end of the pipe held the shape while sinking down in the water, due to reduced wetting between water and alumina. One can observe the same by adding alumina to cryolite [37], but this is due to the rapid freezing of bath around the particles.

In water, both the viscosity and in particular the surface tension is much lower compared to cryolite. It is not possible to state by the water model if the surface tension and density of cryolite alone will hold particles afloat. One should try to find another liquid that have properties more similar to cryolite.

A cold model could give relevant information that about phenomena that cannot be observed in industrial or laboratory cells. Improvements of the model will be to find a liquid with more similar properties. The model will also be more relevant if rapid freezing of bath upon alumina addition is considered. A possible approach will be to freeze alumina and add it into a bath which is close to liquidus, for example water around 0 °C. It should also be possible to have convection and bubbles, in order to get conditions more similar to those found in industrial cells.

4. Experimental work

4.1 Background

The literature review in chapter 2 show that more experiments should be carried out. This work done is based on the work of Walker et al. [37], Kaszás et al. [16] and Kobbeltvedt [18]. The goal of the experiments can be summarized to:

- Develop a reproducible method that can be used to create and fetch floating rafts in a laboratory cell.
- Investigate variation of mass and composition of layers for rafts as a function of time.
- Investigate how a difference in bath temperature affects the raft formation.

4.2 Setup

The experiment was done in a custom-made furnace which is open in the top. It consists of a steel pipe with a diameter of 15 cm and a height of 31 cm. It is heated by a heating element that goes in a spiral around the pipe. During experiments, the top of the pipe was covered with insulation in order to preserve heat. The furnace can be used for temperatures up to 1200 °C. Image and a sketch of the furnace are shown in figure 4.1.

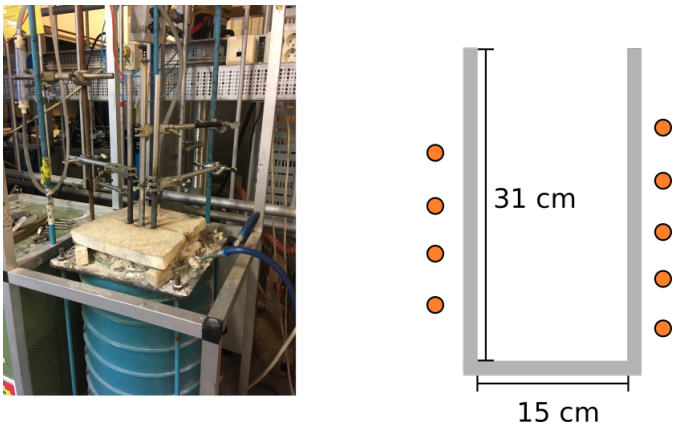

Figure 4.1: Image and sketch of the furnace used for experiments.

A special designed ladle in stainless steel was used to fetch the rafts. A sketch of the ladle is shown in figure 4.2, and an image in figure 4.3. Feeding was done through a 50 cm long and 1 cm in diameter pipe. A lid was mounted on the bottom of the pipe. The lid was opened with a spring feather button on the top of the pipe. Detailed images can be seen in figure 4.4.

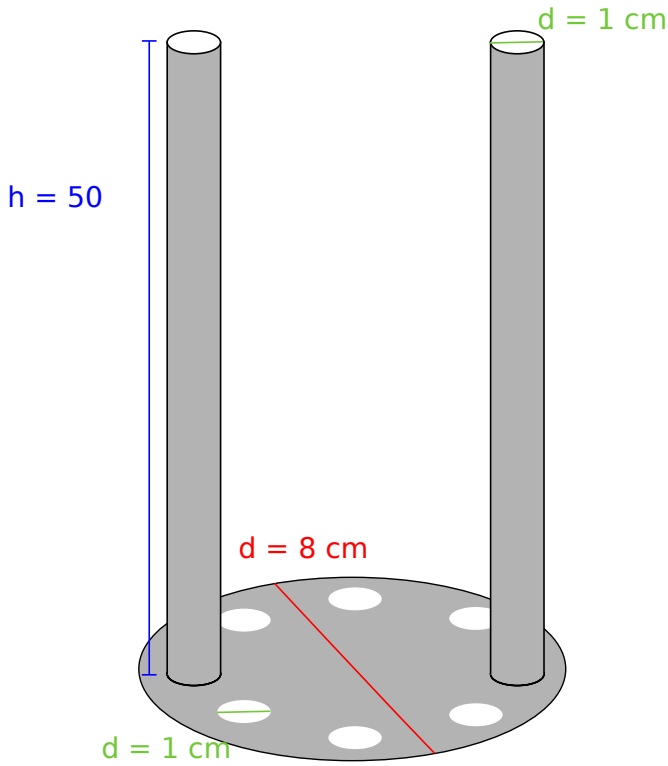

Figure 4.2: Sketch of the ladle used with dimensions.

Figure 4.3: Image of one of the ladle used.

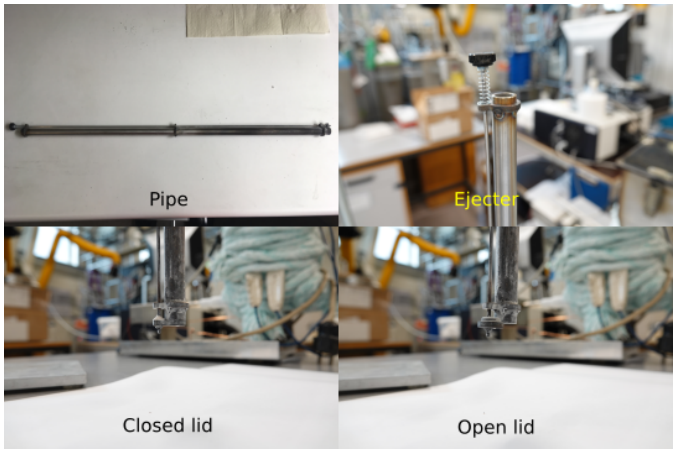

Figure 4.4: Images of the feeding pipe used in the experiments.

A carbon crucible with inner diameter of 10.5 cm and height of 15 cm was used. The crucible was filled with approximately 1300 g of industrial bath, with properties given in table 4.1. The ladle was weighed and then immersed slowly into the bath in order to avoid rapid freezing. Temperature was monitored using a thermocouple in a closed steel pipe, which was immersed into the bath. Nitrogen was purged into the furnace with an alumina pipe in order to inhibit oxidation of the carbon crucible. Sketch of the setup are shown in figure 4.5, and an image in figure 4.6.

Table 4.1: Physical data for the industrial cryolite used.

Property	Value
Bath acidity	10.8 wt%
Alumina content	3.8 wt %

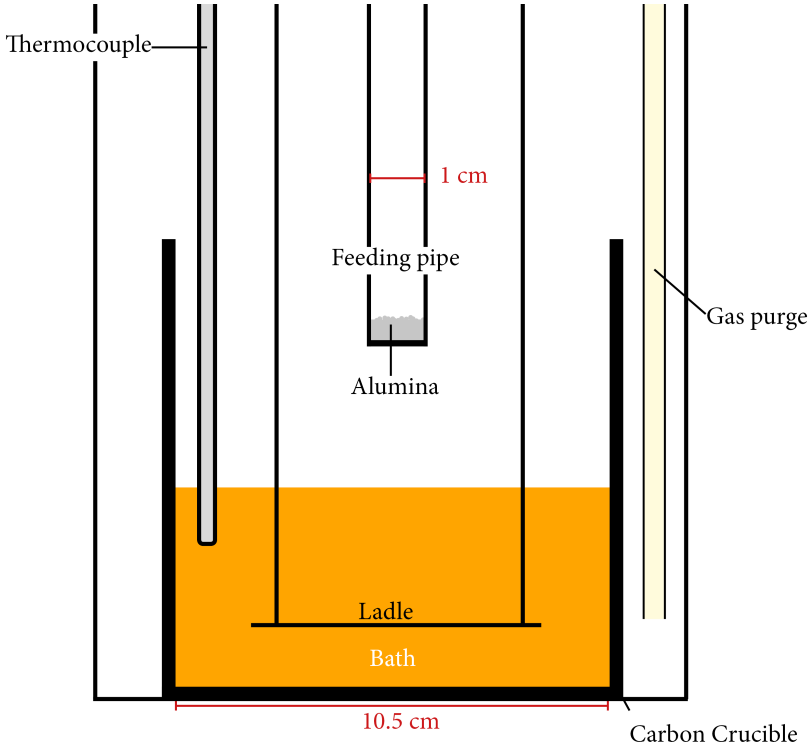

Figure 4.5: Vertical cross section of the experimental setup.

Figure 4.6: Photograph of the setup seen from above.

4 g Industrial secondary alumina from Alcoa Mosjøen was used in each run. Properties of the primary alumina, i.e. before it goes through the dry scrubbing process, is given in table 4.2. Alumina was poured into the closed feeding pipe. When a stable temperature was reached, the pipe was placed into to the furnace, such that the end of the pipe was about 5 cm over the bath surface. Alumina was ejected a few seconds after the feeding pipe was placed. After a certain time, between 30 and 300 seconds, the ladle was withdrawn from the crucible. The ladle was cooled inside the furnace for 2 to 3 minutes, before removed and cooled further on a steel plate.

Table 4.2: Physical data for the industrial alumina used.

Property	Value
< 149 µm	3.2
44-149 µm	89.1
> 44 µm	7.7
L.O.I. (300 °C- 1000 °C)	0.52 %
Surface Area (m2/g)(BET)	72.5
Alpha Alumina	3.4 %

4.3 Image analysis

After cooling, the ladle with sample and the sample removed from the ladle were weighed. All samples were photographed with a Sony DSC-RX10M4 camera. The surface area of the samples was measured by processing the images in imageJ.

4.4 Light microscopy

Five samples were chosen out for light microscopy. Samples were cracked apart in order to observe the cross section of the sample. They were molded in Clarocit and ground on Holder Hartman ATM Saphir 360 with AKASEL Rhaco Grit grinding paper with three different grit sizes: 220, 500 and at last 2500. The samples were then polished with AKSAL Polishing Cloths.

Rectified ethanol was used a cooling agent in the grinding and polishing process, as water could destroy the samples.

The samples were observed in a Nikon SMZ 800N Light microscope. Images were taken at 1X and 8X.

5. Experimental results

5.1 Mass and area measurements

At least three samples for each time were taken and the error bars drawn assume a Student's t-distribution within an confidence interval of 95 %. Results from 945 °Ccontain no error bar as only one measurement per time was done. The mass gain of the sample as a function of time is shown in figure 5.1. Regression was done by assuming a second order polynomial curve. However, the line became so straight that one can express the regression as a linear curve, with a slope of 0.8 g/min.

Surface area of the rafts as a function of time is shown in figure 5.2.

Figure 5.3 show the area as a function of mass gain.

5.2 Light Microscopy

Figure 5.4 shows two images of the alumina used in all experiments.

Figures 5.5-5.9 show images of cross section of 5 different samples.

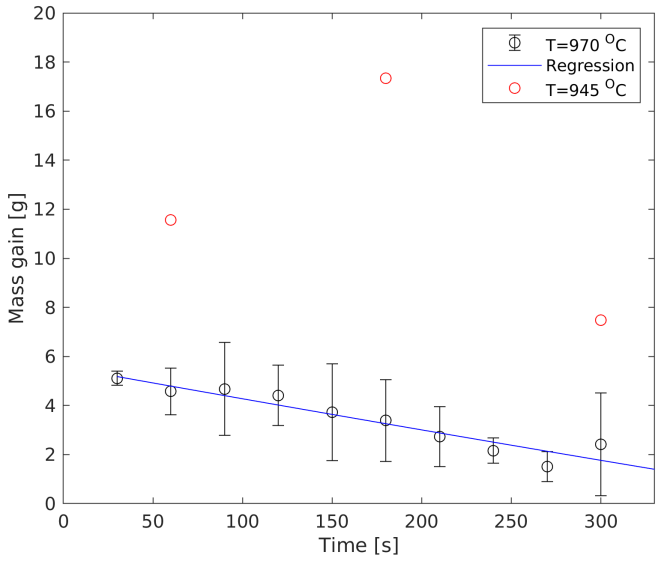

Figure 5.1: Measurements of the mass gain of samples as a function of time. The error bars are within 95 % confidence interval. Regular values are measurement at 970 °C, while the red values are mass gain for samples obtained at 945 °C.

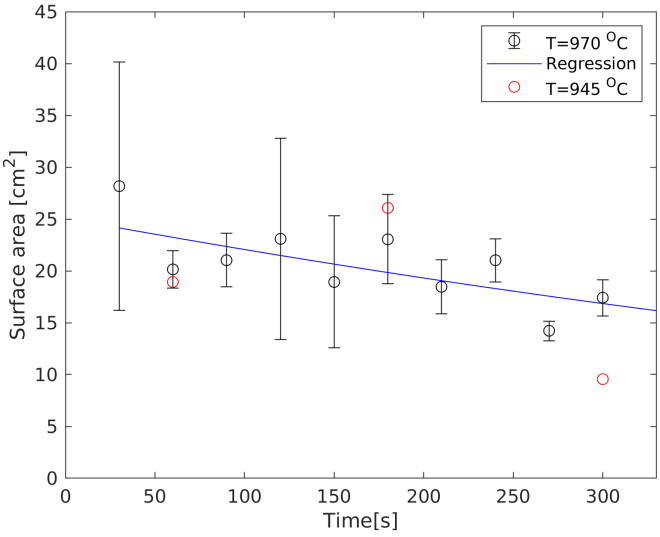

Figure 5.2: Measurements of the surface area of samples as a function of time. The error bars are within 95 % confidence interval. Regular values are measurement at 970 °C, while the red values are mass gain for samples obtained at 945 °C.

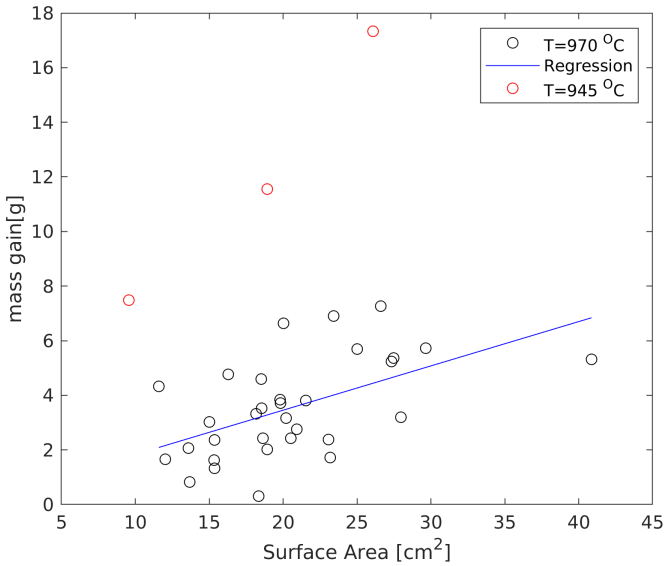

Figure 5.3: Plot of surface areas as a function of mass gain.

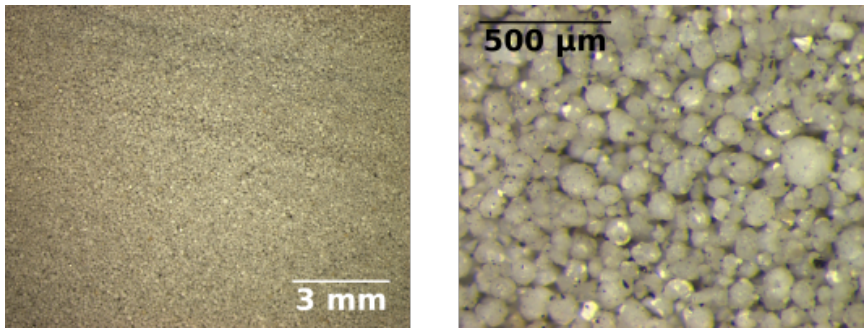

Figure 5.4: Light microscope image of alumina used for experiment.

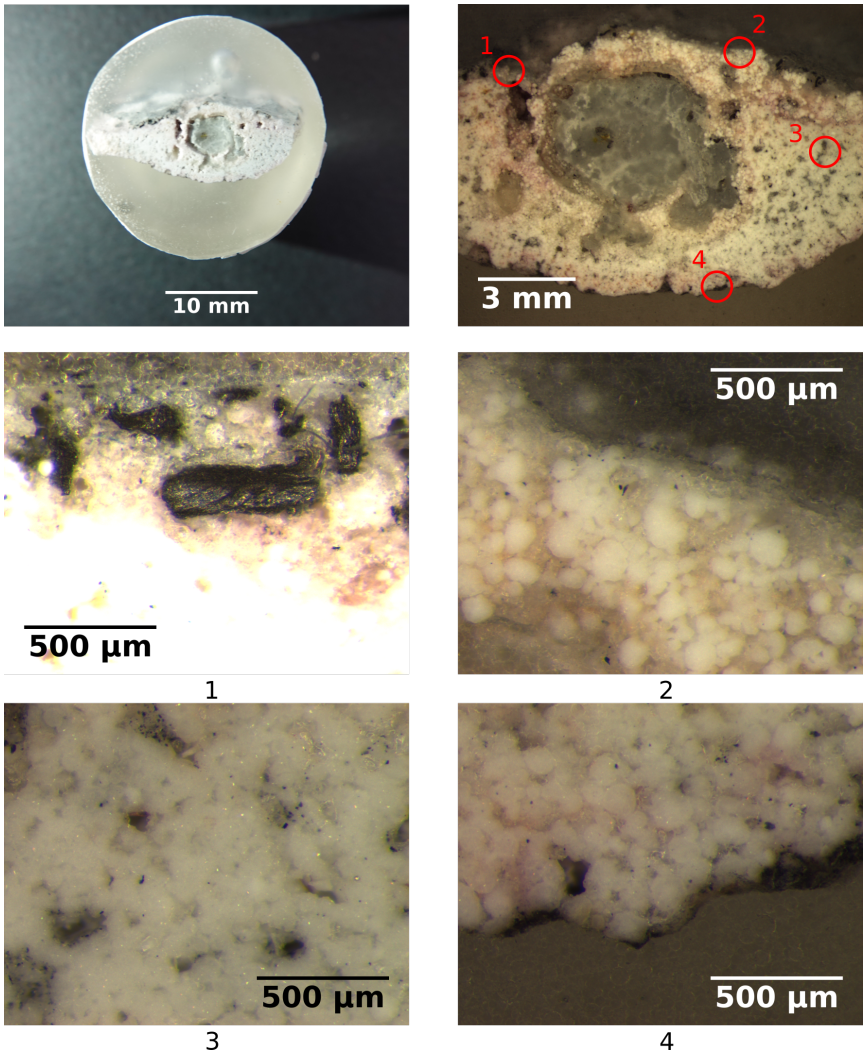

Figure 5.5: Images of sample collected after 300 s at 970 °C.

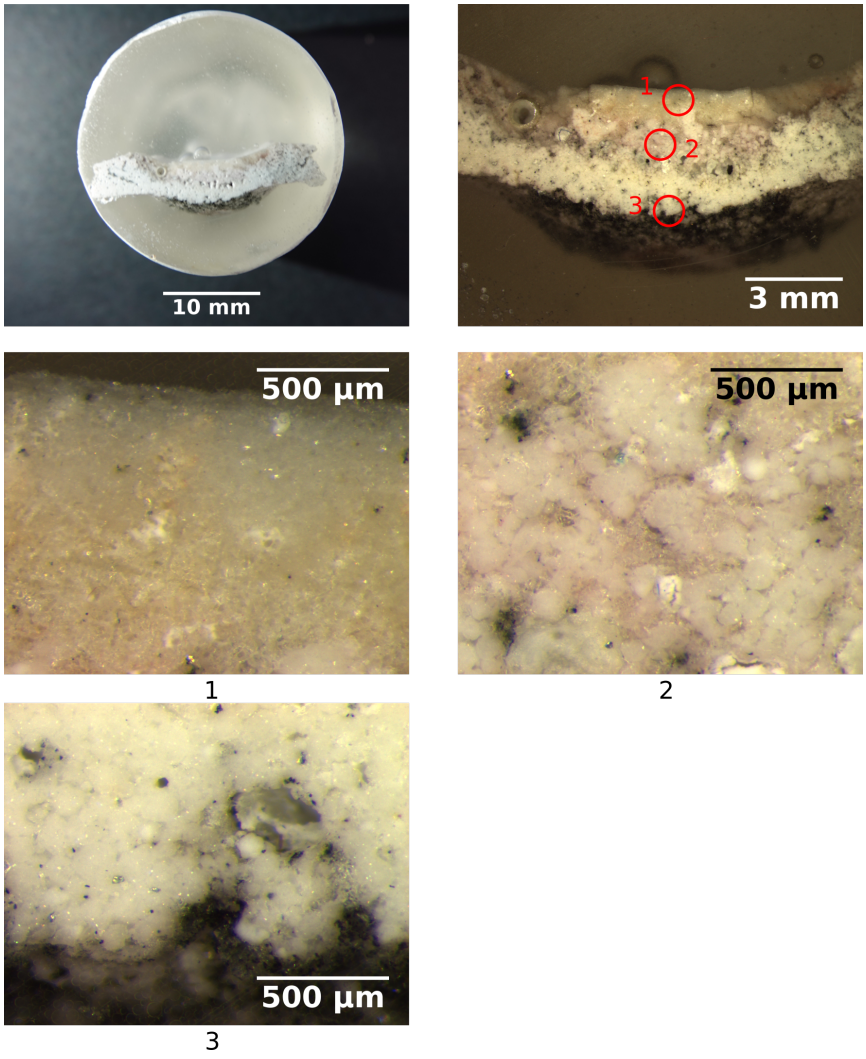

Figure 5.6: Images of sample collected after 90 s at 970 °C.

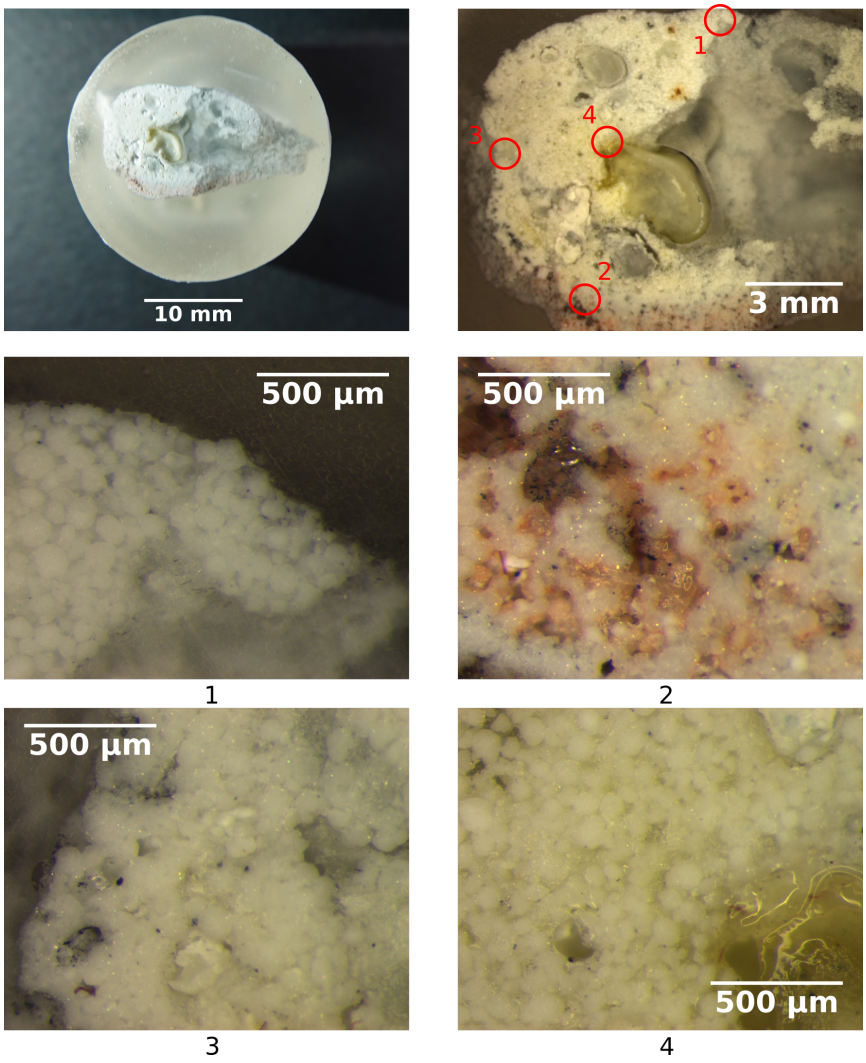

Figure 5.7: Images of sample collected after 60 s at 970 °C.

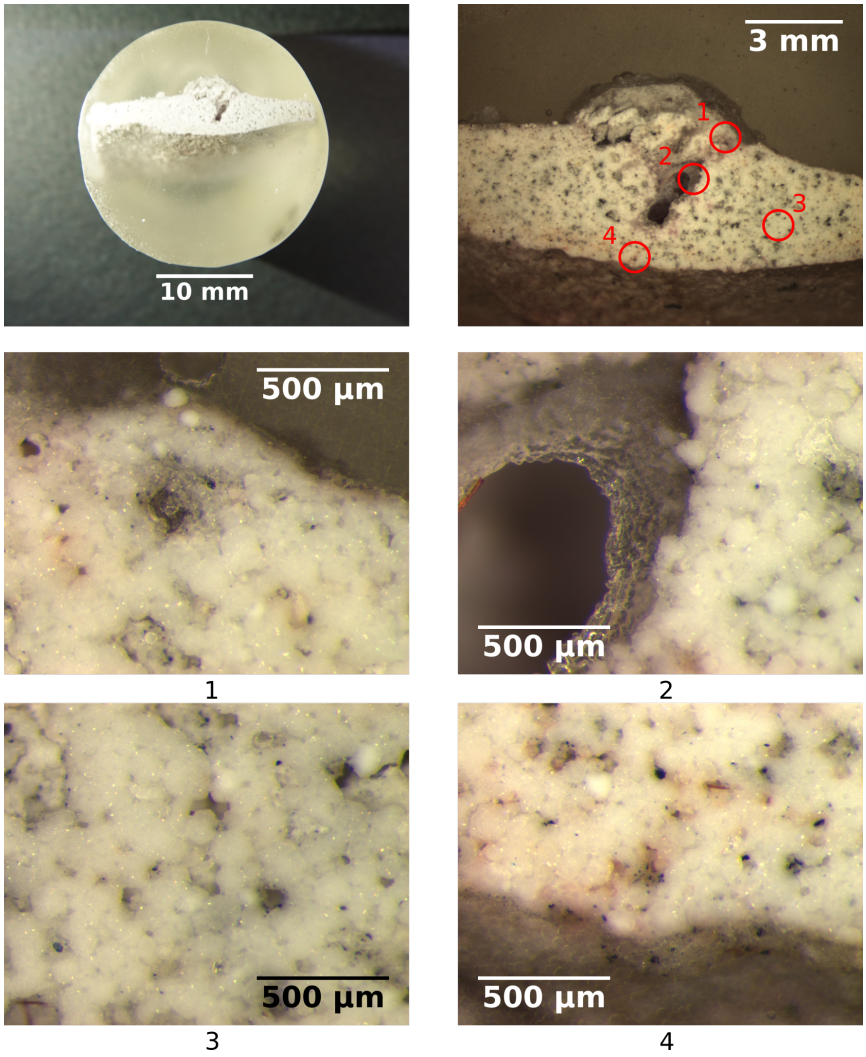

Figure 5.8: Images of sample collected after 180 s at 970 °C.

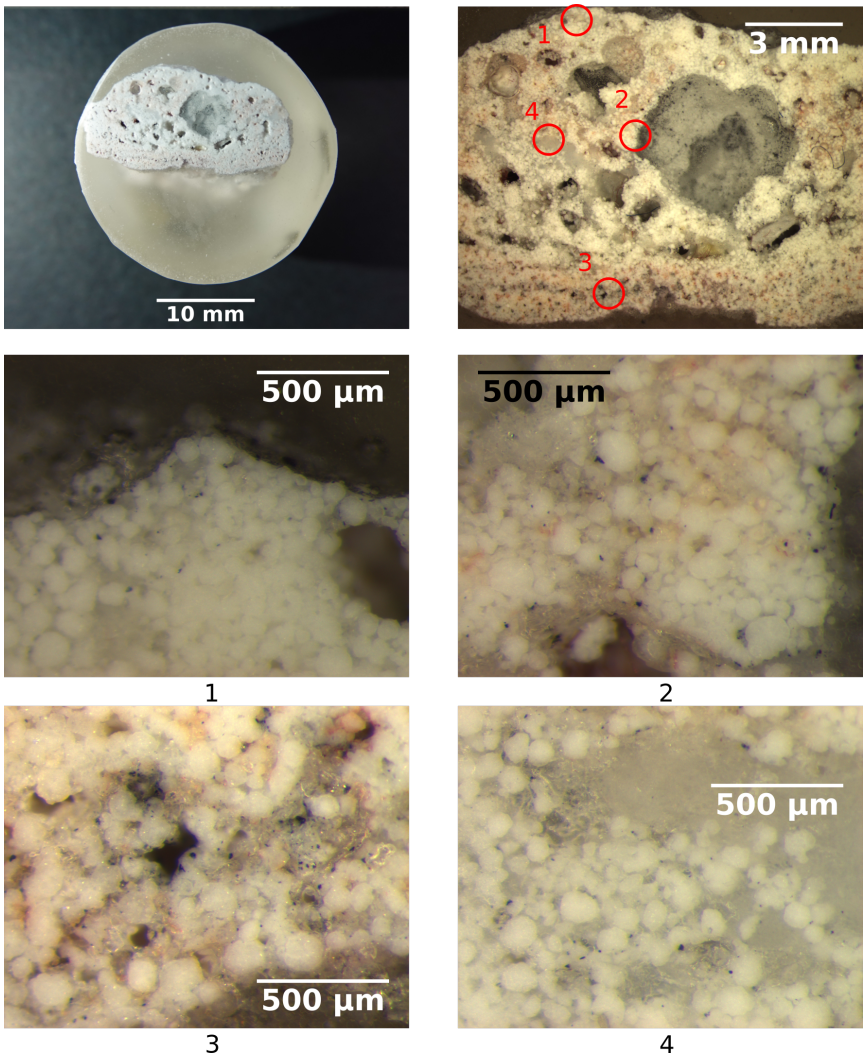

Figure 5.9: Images of sample collected after 180 s at 945 °C.

6. Theoretical framework

Simulations can be a useful tool in gaining understanding of the formation and breakup of rafts, without needing to perform complicated and dangerous experiments. This chapter gives a description of multiphase flow and Computational Fluid Dynamics, which is foundation for the current simulation done in this thesis. The theory is explained in earlier work [11], but indeed in revised form here for the scale of completeness.

6.1 Fluid mechanics

Fluid dynamics can be used to explain the feeding of alumina particles from the feeder and into the cryolitic bath. When the particle falls from the feeder and down to the bath. Newton's laws of motion applies. If considering the particles to be a fluid, equations that explains the behavior can be derived. In the following section, equations for a single compressible flow is derived.

The equation of continuity

In order to the derive this equation, we consider a control volume as shown in figure 6.1

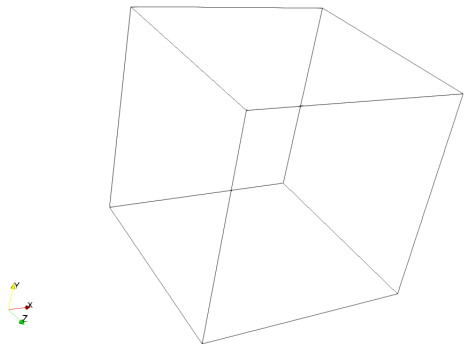

Figure 6.1: Sketch of the control volume.

Considering a fluid flowing through the control volume, one can set up a balance stating that the mass flow in - the mass flow out + reacted = the accumulated mass

$$\begin{aligned}&(\dot{m}_x(x,y,z)-\dot{m}_x(x+\Delta x,y,z))\Delta y\Delta z\\&+(\dot{m}_y(x,y,z)-\dot{m}_y(x,y+\Delta y,z))\Delta x\Delta z\\&+(\dot{m}_z(x,y,z)-\dot{m}_z(x,y,z+\Delta z))\Delta x\Delta y\\&+\dot{R}\Delta x\Delta y\Delta z=\frac{\partial m}{\partial t}=\frac{\partial \rho}{\partial t}\Delta x\Delta y\Delta z\end{aligned} \tag{6.1}$$

here, the $\dot{m}_i$ is the mass fluxes in the i-direction and m is the mass. $\dot{R}$ is a rate of production the fluid per volume, given in kg/(s m^3). In the last term, the mass is sett to be the density times the volume. Dividing equation (6.1) by the volume, and let $\Delta x, \Delta y$ and Δz go to zero, one get

$$-\left(\frac{\partial \dot{m}_x}{\partial x}+\frac{\partial \dot{m}_y}{\partial y}+\frac{\partial \dot{m}_z}{\partial z}\right)+\dot{R}=\frac{\partial \rho}{\partial t}=-\nabla\cdot\dot{\boldsymbol{m}}+\dot{R} \tag{6.2}$$

The reaction rate $\dot{R}$ is written on per volume basis, and $\dot{\boldsymbol{m}}=[\dot{m}_x,\dot{m}_y,\dot{m}_z]$. Finally, by writing $\dot{\boldsymbol{m}}$ as $\rho\boldsymbol{u}$, where $\boldsymbol{u}$ is the velocity, one finally obtain the continuity equation:

$$\frac{\partial \rho}{\partial t}+\nabla\cdot(\rho\boldsymbol{u})=\dot{R} \tag{6.3}$$

Momentum balance

A momentum balance can be seen as Netwton's 2nd law of motion.

$$m\boldsymbol{a}=\sum(\boldsymbol{F}_i) \tag{6.4}$$

where $\boldsymbol{a}$ is the acceleration vector and $\boldsymbol{F}_i$ are forces acting on the body. Considering the control volume in figure 6.1 and let all the sides goes towards zero, and defining $\boldsymbol{a}=\frac{d\boldsymbol{u}}{dt}$, equation (6.4) can be written as

$$\frac{d}{dt}\int_{CV}\rho\boldsymbol{u}dV=\sum(\boldsymbol{F}_i) \tag{6.5}$$

over a control volume CV. Mass is written as the density times the volume.

The forces on the right hand side of (6.5) can be divided up in two parts:

$$\sum(\boldsymbol{F}_i)=\boldsymbol{F}^b+\boldsymbol{F}^s \tag{6.6}$$

where $\boldsymbol{F}^b$ is the body forces and $\boldsymbol{F}^s$ is the surface forces. The forces from the body would be external forces, for example gravity and a change in mass due to reactions. A simplified equation can then be written

$$\boldsymbol{F}^b = \int_{CV} \left(\rho \boldsymbol{f} + \dot{R}\boldsymbol{v}\right) dV \tag{6.7}$$

$\boldsymbol{f}$ are external forces, for example gravity, and $\boldsymbol{v}$ represents the velocity where mass transfer occurs, for example diffusion. The surface term will be a sum of all the momentum entering and leaving the control volume. If the control volume is infinitely small, $\boldsymbol{F}_s$ can be written as

$$\boldsymbol{F}^s = \int_{CS} \boldsymbol{T} \cdot \boldsymbol{n} dA \tag{6.8}$$

CS is control surface area and $\boldsymbol{n}$ is the normal vector out of the area, By applying the divergence theorem. Equation (6.8) can be rewritten as.

$$\int_{CS} \boldsymbol{T} \cdot \boldsymbol{n} dA = \int_{CV} \nabla \cdot \boldsymbol{T} dV \tag{6.9}$$

One can rewrite

$$\frac{d\boldsymbol{u}}{dt} = \frac{\partial \boldsymbol{u}}{\partial t} + \frac{\partial \boldsymbol{u}}{\partial x}\frac{\partial x}{\partial t} + \frac{\partial \boldsymbol{u}}{\partial y}\frac{\partial y}{\partial t} + \frac{\partial \boldsymbol{u}}{\partial z}\frac{\partial z}{\partial t} =$$

$$= \frac{\partial \boldsymbol{u}}{\partial t} + (\boldsymbol{u} \cdot \nabla)\boldsymbol{u} \tag{6.10}$$

then (6.5) can be written as:

$$\int_{CV} (\rho \frac{\partial \boldsymbol{u}}{\partial t} + \dot{R}(\boldsymbol{u} - \boldsymbol{v}) - \nabla \cdot \boldsymbol{T} - \rho \boldsymbol{f} + \boldsymbol{u}(\nabla \cdot \boldsymbol{u}))dV = 0 \tag{6.11}$$

Assuming continuity over the integrand, equation (6.11) can be written in differential form:

$$\rho \frac{du}{dt} + \boldsymbol{u}(\nabla \cdot \boldsymbol{u}) = \dot{R}(\boldsymbol{u} - \boldsymbol{v}) + \nabla \cdot \boldsymbol{T} + \rho \boldsymbol{f} \tag{6.12}$$

which is a common form of Navier Stoke's equation.

The stress tensor

The stress tensor is a part of the momentum balance above, and deserves more attention. A stress sensor is needed in order to explain the surface stresses. Çengel and Cimbala [8] defines the stress tensor as

$$\boldsymbol{T} = \begin{pmatrix} \sigma_{xx} & \sigma_{xy} & \sigma_{xz} \\ \sigma_{yx} & \sigma_{yy} & \sigma_{yz} \\ \sigma_{zx} & \sigma_{zy} & \sigma_{zz} \end{pmatrix} \tag{6.13}$$

where σ_{ij} is the amount of force in the j-direction acting on the face with a normal in i-direction. The diagonal components are called normal stresses, which is a sum of pressure forces and viscous stresses, while the off-diagonal components is only components of shear stresses, since pressure only can act normal to the surface. Equation (6.13) can therefore be written as

$$\boldsymbol{T} = \begin{pmatrix} -p & 0 & 0 \\ 0 & -p & 0 \\ 0 & 0 & -p \end{pmatrix} + \begin{pmatrix} \tau_{xx} & \tau_{xy} & \tau_{xz} \\ \tau_{yx} & \tau_{yy} & \tau_{yz} \\ \tau_{zx} & \tau_{zy} & \tau_{zz} \end{pmatrix} \tag{6.14}$$

p is the pressure and τ_{ij} is called the viscous stress tensor.

This expression does not look easier than equation (6.13). However, fluid models can be used to describe the viscous stress. One of the simplest models are a Newtonian fluid, defined by Çengel and Cimbala [8] to be fluid for which shear stress is linearly proportional to shear strain rate. In addition, if the fluid is assumed to be incompressible, the viscous stress tensor can be written as

$$\tau_{ij} = \mu \left(\frac{\partial \boldsymbol{u}_i}{\partial x_j} + \frac{\partial \boldsymbol{u}_j}{\partial x_i} \right) \tag{6.15}$$

where μ is the dynamic viscosity, and the velocity $\boldsymbol{u}_i$ is differentiated with the respect to the j-direction.

Inserting the expression from equation (6.14) into (6.12), the expression becomes

$$\rho \frac{du}{dt} + \boldsymbol{u}(\nabla \cdot \boldsymbol{u}) = \dot{R}(\boldsymbol{u} - \boldsymbol{v}) + \nabla \cdot \left(p + \boldsymbol{\tau} \right) + \rho \boldsymbol{f} \tag{6.16}$$

where $\boldsymbol{\tau}$ is the second term on right hand side in equation (6.14)

6.2 Multiphase flow

Multiphase flow occur frequently in nature as well as in industrial processes. A phase is defined in Atkins and Paula [1] as "a form of matter that is uniform throughout in chemical composition and uniform state." In an aluminum electrolysis cell, there will be air, cryolite and alumina, as well as other gases and liquids, and it is therefore a multiphase system. The different phases will usually have different properties and new models are needed to describe the system. This section will give an overview of models and equations describing a multiphase system.

In a multiphase system an expression for the phase fraction is needed. A normal definition of this is with respect to volume:

$$\alpha_k \equiv \frac{V_k}{V} \tag{6.17}$$

where V_k is the volume occupied by the k-th phase, and V is the total volume of the system.

Since all volume must be occupied by one phase, the following expression must be fulfilled

$$\sum_k \alpha_k = 1 \tag{6.18}$$

An illustration of a simple two phase system containing only one liquid and one gas is shown in figure 6.2.

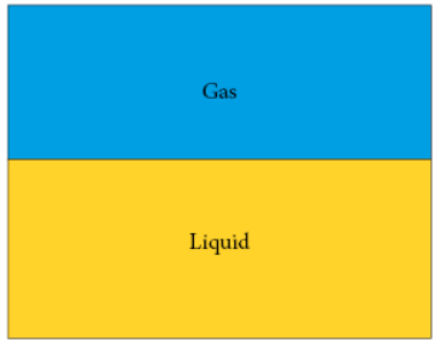

Figure 6.2: Sketch of a simple twophase system containing one gas and one liquid.

Here the fraction of the gas phase, α_g can be calculated by equation (6.17)

$$\alpha_g = \frac{V_g}{V_g + V_l} \tag{6.19}$$

where V_g and V_l is the volume occupied by gas and liquid, respectively. The fraction of liquid can be easily calculated by using the relation from equation (6.18)

$$\alpha_l = 1 - \alpha_g \tag{6.20}$$

The total mass of the k-th phase of the volume is given as

$$m_k = \int \hat{\rho}_k dV \tag{6.21}$$

$\hat{\rho}_k$ is the density of the component k per total volume, and is defined as

$$\alpha_k \rho_k = \hat{\rho}_k \tag{6.22}$$

By using equation (6.3), a balance for each phase can be expressed, replacing ρ by $\hat{\rho}_k$. By also applying the definition given in equation (6.22), the mass conservation for each phase can be expressed as

$$\frac{\partial(\alpha_k \rho_k)}{\partial t} + \nabla \cdot (\alpha_k \rho_k \boldsymbol{u}_k) = \dot{R}_k \tag{6.23}$$

This can also be done for the momentum balance

$$\frac{\partial(\alpha_k \rho_k \boldsymbol{u}_k)}{\partial t} + \nabla \cdot (\alpha_k \rho_k \boldsymbol{u}_k \boldsymbol{u}_k) = \dot{R}_k \boldsymbol{v}_k + \nabla \cdot (\alpha \boldsymbol{T}_k) + \alpha_k \rho_k \boldsymbol{f}_k + \boldsymbol{M}_k \tag{6.24}$$

$\boldsymbol{M}_k$ is a new term here, which is the force per volume acting on the phase due to interaction with other phases. An example of such a force is surface tension, were the fluids tends to contract together due to differences in attractive forces.

By assuming isothermal condition, there is no need to consider the energy equation.

Equation (6.23) and (6.24) must be solved for every phase, creating in total 4N-1 equations for a system with N phases. This assumes that the term $\boldsymbol{M}_k$ known. However, in most cases a model must be used, giving even more equations to be solved.

Volume of fluid

The Volume of Fluid (VOF) model, developed by Hirt and Nichols [13] gives a method to model the interactions between phases. Fluid properties in a system is modeled using a weighting function, in this case the volume fraction. The density ρ will then be expressed as

$$\rho = \sum_{k=1}^{N} \alpha_k \rho_k \tag{6.25}$$

for a system consisting og n phases. This can also be done for the dynamic viscosity μ.

α_k can be calculated from the transport equation

$$\frac{\partial}{\partial t}(\alpha_k \rho_k) + \nabla \cdot (\alpha_k \rho_k \boldsymbol{u}) = 0 \tag{6.26}$$

assuming that no reactions occur. This equation must be solved for $N-1$ phases. The last phase is found by the relation in equation (6.18).

If assuming an incompressible system, the equation of continuity can be written as

$$\nabla \cdot \boldsymbol{u} = 0 \tag{6.27}$$

And the momentum equation is

$$\frac{\partial}{\partial t}(\rho \boldsymbol{u}) + \nabla(\rho \boldsymbol{u}\boldsymbol{u}) = -\nabla P + \nabla \boldsymbol{\tau} + \rho \boldsymbol{f} \tag{6.28}$$

The areas where phases are mixed, equation (6.26) is used to calculate volume averaged values of ρ and μ, assuming a Newtonian fluid. Then the momentum equation is then solved for with these averaged values. This yields a system of total $3+N$ equations, and is therefore easier to solve.

6.3 Computional Fluid Dynamics

The equations described in previous sections are a set of nonlinear partial differential equations, which rarely have an analytical solution. Computational Fluid Dynamics (CFD) applies numerical methods in order to give detailed descriptions of the practical problems. This chapter contains a overview to the concepts of CFD, with focus on the subjects relevant for this thesis. A more detailed introduction to CFD can be found in Versteeg and Malalasekera [35].

Mesh

A computer is discrete by nature, and the values must therefore be defined in points instead of being a continuous value. This yields a set of values at certain points, and interpolation will be used to describe the values between these. The user can set the location and amount of these points by creating a mesh. Illustration of an easy mesh in two dimension is shown in figure 6.3. Figure 6.4 shows a sketch for one individual cell. In each cell, momentum balances and conservation laws will be solved. The cells have faces, defining the border between them. If the point are on the edges of the system, the face value must be defined through boundary conditions. More points will give a denser mesh. The momentum balance and conservations laws must then be solved at even more locations, resulting in higher computational time due to an increased amount of equations that needs to be solved, but also more accurate solutions.

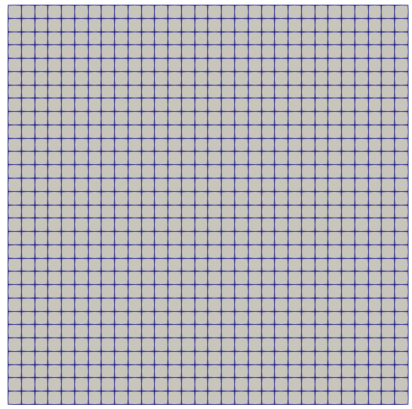

Figure 6.3: Example of a mesh in two dimension, in total 900 cells.

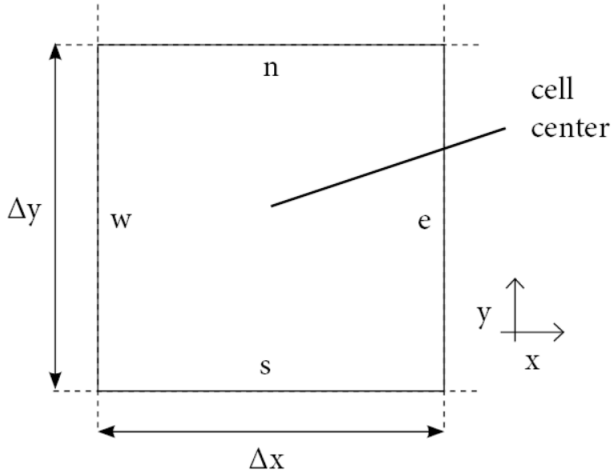

Figure 6.4: Sketch of an 2D cell. The cell is surrounded with four faces denoted e,s,w and n. n and s will have a surface area Δx, while the area for w and e is Δy.

The finite volume method

The finite volume method is a commonly used method in CFD. The main feature of this method is that the equations is solved on integral form. An example, also used by Versteeg and Malalasekera [35] is the incompressible steady-state equation:

$$\int_{CV} \nabla \cdot \boldsymbol{u} dV = \int_{CS} \boldsymbol{u} \cdot \boldsymbol{n} dS = 0 \tag{6.29}$$

The divergence theorem has been applied at equation (6.29). Considering a 2D-case, the velocity at a face f can be written in vector notation:

$$\boldsymbol{u}_f = [u_f, v_f] \tag{6.30}$$

Using the same cell as showed in figure 6.4, (6.29) can be written as

$$-u_e \Delta y - v_s \Delta x + u_w \Delta y + v_n \Delta x = 0 \tag{6.31}$$

The system will consists of several cells, where each cell will have an equation on the same form as equation (6.31). This will yield a system of simultaneous algebraic equations.

The problem can then be formulated as an equation on matrix form.

$$\boldsymbol{A} \cdot \boldsymbol{x} = \boldsymbol{y} \tag{6.32}$$

Where $\boldsymbol{A}$ is the system matrix while $\boldsymbol{x}$ is a vector of unknowns. $\boldsymbol{y}$ is a vector containing values independent of the unknowns is located. The solution will be to invert the matrix. However, in normal cases, the matrix will consist of several millions entries, making a direct inversion method hard to apply. Iterative methods can, and sometimes must, be used in order to inverse the matrix. Discussion of iterative methods are beyond the scope of this project. Detailed descriptions and algorithms can be found in Kreyszig [20] or Versteeg and Malalasekera [35].

Spatial discretization

The conservation laws must also be solved individual for each cell. A general conservation law for a scalar quantity ϕ can be expressed as

$$\nabla \cdot (\rho \boldsymbol{u} \phi) = \nabla \cdot (\Gamma \nabla \phi) + S_\phi \tag{6.33}$$

The term of left hand side represent convection. On the right hand side, the first term is transport due to diffusion, and S_ϕ is a source term. Γ is a diffusion coefficient. Setting Γ=0, $S_\phi = \dot{R}$, and $\phi = 1$, one obtains the equation of continuity (6.3).

The integral form of equation (6.33) will be

$$\int_{CS} (\rho \boldsymbol{u} \phi) \cdot \boldsymbol{n} dS = \int_{CS} (\Gamma \nabla \phi) dS + \int_{CV} S_\phi dV \tag{6.34}$$

where the divergence theorem is applied on the two first terms in order to get them as surface integrals. This equation must be solved for every cell in the mesh.

Considering a mesh as in figure 6.3, and using the notation as illustrated in figure 6.5, equation (6.34) can be discretized

$$\int_{CS} (\rho \boldsymbol{u} \phi) \boldsymbol{n} dS = (\rho_e u_e \phi_e) A_e - (\rho_w u_w \phi_w) A_w + (\rho_n u_n \phi_n) A_n - (\rho_s u_s \phi_s) A_s \tag{6.35}$$

In this system $A_e = A_w = \Delta y$ and $A_n = A_s = \Delta x$. The diffusion term becomes

$$\int_{CS} (\Gamma \nabla \phi) = \left(\Gamma_e \frac{\partial \phi}{\partial x}\Big|_e - \Gamma_w \frac{\partial \phi}{\partial x}\Big|_w \right) \Delta y + \left(\Gamma_n \frac{\partial \phi}{\partial y}\Big|_n - \Gamma_s \frac{\partial \phi}{\partial y}\Big|_s \right) \Delta x \tag{6.36}$$

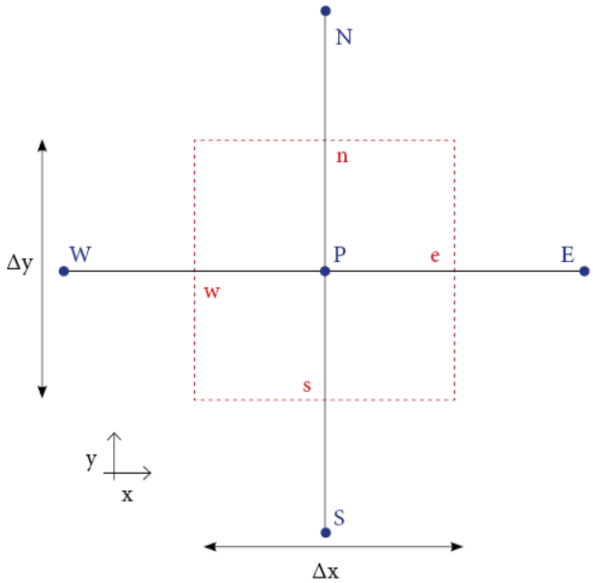

Figure 6.5: Sketch of a cell center or node P, with faces w, s, e and n , as well as neighbouring cell centers W, S, E and N.

and the source term will be written as its volume average

$$\bar{S}_{\phi p} = \frac{1}{\Delta V} \int_{CV} S_\phi dV \tag{6.37}$$

In total, the discretized version of equation (6.34) will be

$$\sum_f \rho_f u_f \phi_f A_f = \sum_f \Gamma_f \nabla \phi_f A_f + \bar{S}_{\phi p} \tag{6.38}$$

for a cell center P, summed over all of its neighboring faces f. ϕ_P must be found such that equation (6.38) is fulfilled. ϕ_P will be indirectly involved as values of the faces is not known. One intuitive approximation will be to state that value in one face to be the mean of the neighboring cellcenters. For the western face, it will be

$$\phi_w = \frac{\phi_W + \phi_P}{2} \tag{6.39}$$

This can also be done for Γ, u and ρ. The source term can be linearized.

$$\bar{S}_{\phi P} = S_u + S_P \phi_P \tag{6.40}$$

An easy approximation for the gradient will be central discretization

$$\left.\frac{\partial \phi}{\partial x}\right|_w = \frac{\phi_P - \phi_W}{\Delta x_{PW}} \tag{6.41}$$

where Δx_{PW} is the distance between the points P and W.

An expression for a scalar quantity will be

$$a_P \phi_P = \sum_n a_n \phi_n + S_u \tag{6.42}$$

The coefficients a will depend on values of Γ, ρ and u at the other cell centers. With the the approximations done as explained in equations (6.39) - (6.41), only the closest neighbours will considered:

$$a_P \phi_P = a_W \phi_W + a_S \phi_S + a_E \phi_E + a_N \phi_N + S_u \tag{6.43}$$

However, as discussed by Versteeg and Malalasekera [35], the discretization method used, especially the central differencing, equation (6.41), has several weaknesses. The central differencing scheme does not recognize the direction of the velocity and will only be stable and accurate when the ratio between the convection and diffusion is not too high. Another scheme should therefore be considered. The mean approximation, equation (6.39), has an error of first order, and it should be used a scheme of higher order. Details of the schemes will not be considered here, but many schemes are introduced and detailed explained in [35]. These schemes will normally involve more than only the closest neighboring cell, increasing the n in equation (6.42). The increased number of n will give a matrix $\boldsymbol{A}$ in equation (6.32) with more nonzero entries, giving an even more complex problem to solve.

Pressure velocity coupling

By observing the momentum equation (6.16), the pressure is present, but there exist no equation describing pressure for incompressible fluids. If the pressure field is not known, equation (6.16) cannot be solved directly. If the right pressure field is given, velocities in the momentum equation will also satisfy the equation of continuity, equation (6.3). In CFD, one use an iteration algorithm solve this problem. For a multiphase system, the pressure field and other parameters will first be guessed, and then the

momentum equation will be used to calculate the velocities. Then, the equation of continuity together with the momentum equation is used to create a pressure correction equation. It is then possible to use the corrected pressure field to calculate new velocities and other scalar values, creating an iterative scheme.

PIMPLE Algorithm is frequently used. It is a combination of two other algorithms: PISO (Pressure Implicit with Splitting of Operator) and SIMPLE (Semi-Implicit Method for Pressure-Linked Equations). These two algorithms are explained by Versteeg and Malalasekera [35]. The PIMPLE algorithm is explained by Barton [2].

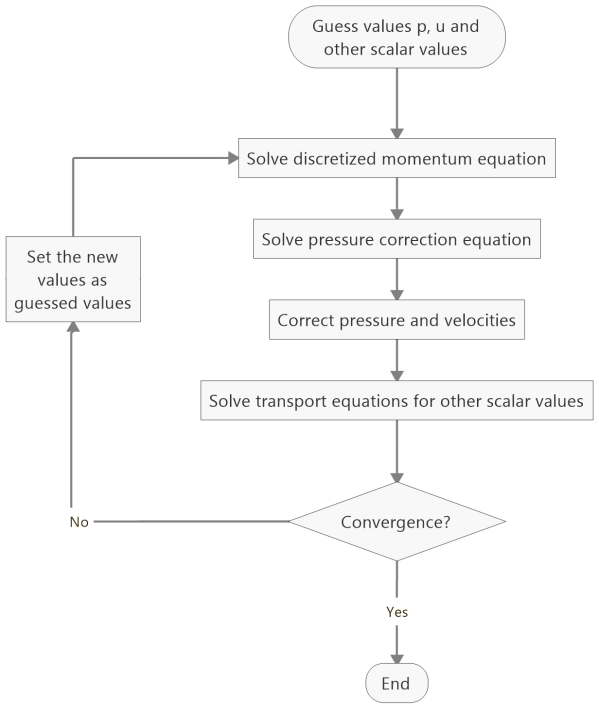

Figure 6.6: Flowchart of a algorithm solving the pressure velocity coupling in an incompressible flow.

Convergence

CFD solves the problems by iterations and these it will stop when reached convergence. Convergence will be at the iteration where the values will not change. Since iterating until none of the values change will take long time, one usually use a tolerance. As explained in OpenCFD [23], for a quantity ϕ, the iterations have reached convergence when

$$\frac{||\phi^n - \phi^{n-1}||}{||\phi^1 - \phi^0||} \leq \epsilon \tag{6.44}$$

ϵ is a tolerance value, usually around 10^{-6}.The iterations will then stop as the difference in values between time step n and $n-1$ quantity is much smaller than the difference between start condition 0 and first iteration value 1. In equation (6.44), the 2-norm error is used, which is given as

$$||\phi|| = \left(\Delta x \Delta y \sum_{i=1}^{NI} \sum_{j=1}^{NJ} \phi_{i,j}^2 \right)^{\frac{1}{2}} \tag{6.45}$$

For a mesh consisting og NI cells in x-direction and NJ cells in y-direction.

The condition of (6.44) is sometimes hard to obtain. Another convergence criterion used is called relative convergence, which occur when

$$\frac{\phi^n}{\phi^0} \leq \lambda \tag{6.46}$$

where λ is the relative tolerance value. The solution has converged when one of the conditions in equation (6.44) and (6.45) are fulfilled.

7. Simulations

The aim is to continue on the model developed in the project work. Aims for this thesis can be summarized to be:

- Create an isothermal Volume of fluid (VOF) model with the same dimensions as the laboratory cell.
- Observe if simulations can give an explanation of phenomena found in laboratory samples.

Since a lab experiment is done, a setup with same dimensions are simulated in OpenFOAM. This chapter contains details about the setup of the simulations, and description of the solver used. The description of the solver is an revised form of earlier work[11].

OpenFOAM is a free, open source simulation platform. It has a wide range of applications, and can be used to solve complex fluid flows involving chemical reactions, heat transfer and turbulence [25]. A drawback is the varying levels of documentation. Files are written in C++ and a user can write a solver from scratch. After a simulation is completed, the data must be visualized in a another program, for example ParaView. OpenFOAM contains several inbuilt solver. The solver used in this work, multiphaseInterFoam, will be used as an example.

7.1 MultiphaseInterFoam

For simulations in current work, a solver called multiphaseInterFoam is used, described as a "Solver for n incompressible fluids which captures the interfaces and includes surface-tension and contact-angle effects for each phase. Turbulence modeling is generic, i.e. laminar, RAS or LES may be selected."[24]. The structure of the solver is shown in figure 7.1 A flow sheet on how the solver works is shown in figure 7.2.

Each solver contains files about how the setup should be, for example numerical methods and mesh. These files are called dictionaries, an are stored in a folder called system. Overview and description of the different dictionaries are shown in table 7.1. Properties, for example transport and turbulence model are stored in a folder named constant. An overview is found in table 7.2 Finally, the information about phase fractions and other variables are that varies through time is stored in folders time-named folders. The phase fraction in each cell is denoted with as α, followed by the name of the phase.

For these simulations, three phases are considered: air, alumina and bath. An overview is shown in table 7.3

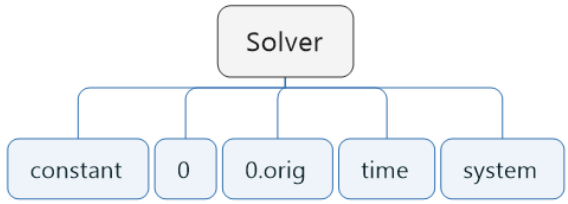

Figure 7.1: Illustration of the different directories in multiphaseInterFoam.

Table 7.1: Overview of files in the system-directory.

Name	Purpose
blockMeshDict	Defines how the mesh of the system should be created
setFieldsDict	Contains information about the initial conditions
fvSolution	States which numerical methods that should be used and the iterations algorithms
decomposeParDict	Contains information about how the system should be divided, if parallel simulations are run
controlDict	States the time interval, writing interval and time step

Table 7.2: Overview of files in the constant-folder.

Name	Purpose
g	State the magnitude and direction of the gravity
motionProperties	States how a mesh should change during simulations
transportProperties	State type of transport model the fluids should have
turbulenceProperties	States turbulence model

Table 7.3: Overview of files in the time-folders.

Name	Description	Remarks
alpha.air	fraction of air	
alpha.alumina	fraction of alumina	
alpha.cryolite	fraction of cryolite	
alphas	collection of all alphas	States boundary conditions
p	Pressure	
phi	volumetric flow	not in initial conditions
p_rgh	Pressure minus hydrostatic pressure	
U	velocity	

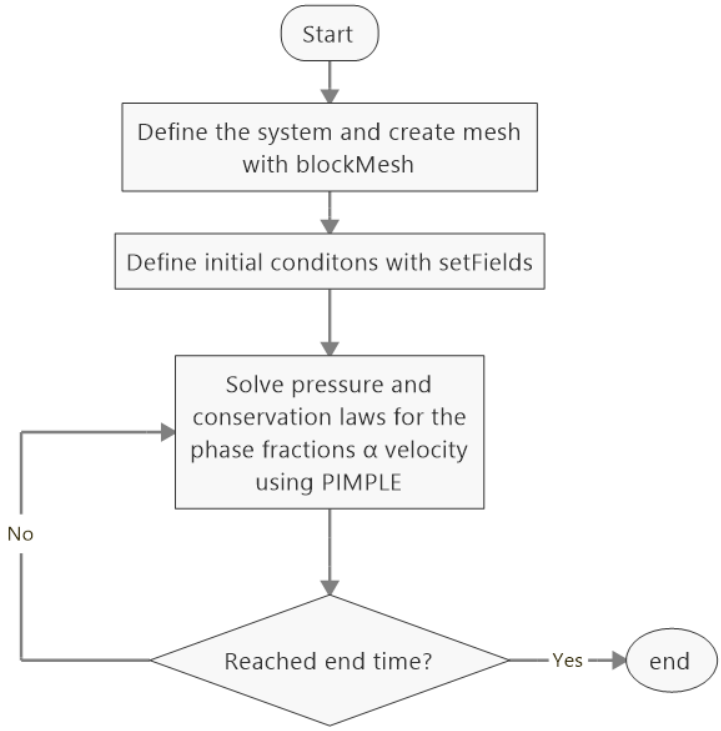

Figure 7.2: Flow sheet illustrating how the solver multiphaseInterFoam works.

7.2 Domain and mesh

A mesh should be fine enough to see the wanted details, but a too fine mesh will lead to high computational times. Most of the interactions are expected to occur in the middle of the crucible and the mesh is therefore be set to be finer there. BlockMesh is a inbuilt mesh-generator in OpenFOAM, which "creates parametric meshes with grading and curved edges"[9]. Setup of the mesh are done in a dictonary called blockMeshDict. The domain should be decomposed into hexahedral blocks. Eight vertices will define each corner of the hexahedron. For each block, OpnFOAM defines a local coordinate system and draws edges between vertex points as described in Greenshields [9].

Edges between the vertices are straight by default, but it is possible to change them to be curved in the dictionary. On the three edges defined as the local coordinate system, the user can define the amount of cell as well as the cell expansion rate in the dictionary. When the command blockMesh is executed, the mesh created is stored as an file in the constant folder.

Blocks were created as by cutting the cylinder in 2 in the middle, illustrated in figure 7.3. Each part was then split in 5 as illustrated in figure 7.4, creating in total 10 blocks. A square is located in the middle, while a graded mesh is drawn around. Curving gives the round shape, while the grading makes it possible to have a dense cell density at the middle of the cell, while the outer sides are coarse. Grading in horizontal direction was done such that the cell density is higher in the interface between cryolite and air. Figure 7.3 illustrate the mesh seen from the side. The mesh used for the simulations is more dense. Mesh properties are set according to table 7.4.

Table 7.4: Summary of mesh properties.

Property	value
Number of cells	1 125 000
Minimum radial spacing	$4.00 \cdot 10^{-4}$ cm
Maximum radial spacing	$4.61 \cdot 10^{-3}$ cm
Minimum horizontal spacing	$9.21 \cdot 10^{-4}$ cm
Maximum horizontal spacing	$3.68 \cdot 10^{-3}$ cm
Spacing square	$4.00 \cdot 10^{-4}$ cm

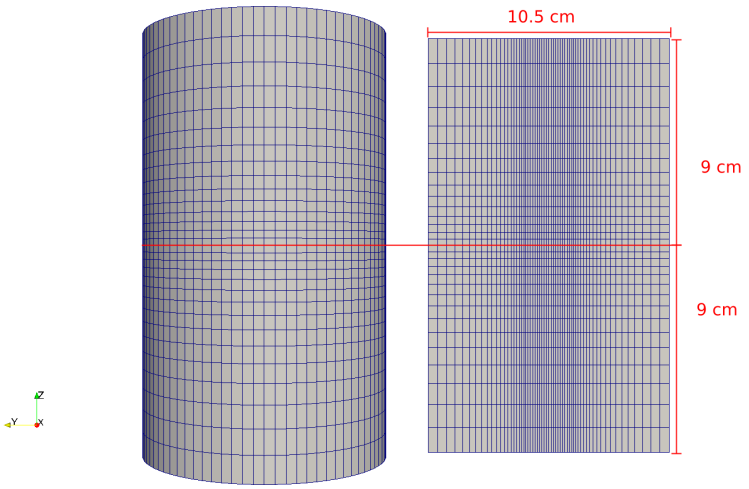

Figure 7.3: Illustration of the mesh genererated, seen from the side. Left shows the mesh from the outside, while right side is a cross section. The horiozontal line indicate where the blocks are split.

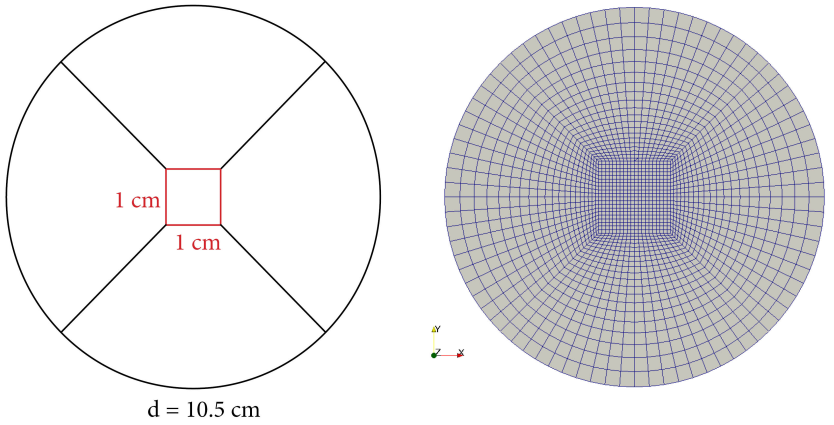

Figure 7.4: sketch of the blocks generated in blockMesh, seen horizontally. Left side shows the blocks, while right side shows a simplified version of the mesh generated.

7.3 Initial conditions

Initial conditions can be set in a dictonary called setFieldsDict. The condition are then set relative to the dimension of the domain and it is therefore not needed to consider the blocks created. Initial condition are then set in the 0-folder when the command setFields is executed.

A cross section with the initial conditions are shown in figure 7.5. The height of alumina is chosen such that the total mass of the alumina dose is four grams.

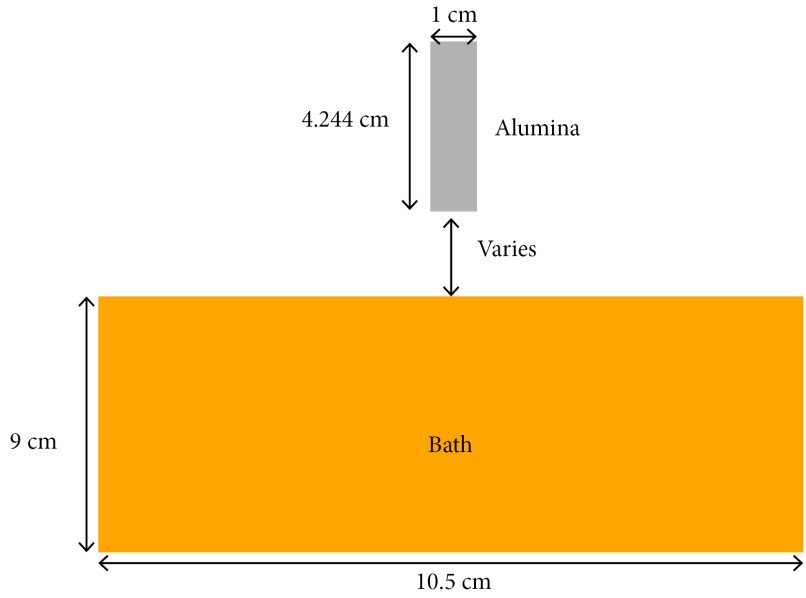

Figure 7.5: Cross section view of the simulation setup. Alumina and bath have a cylindrical shape.

7.4 Boundary conditions

Each property (velocity, pressure, phase) have its own file where information about the boundary condition is defined The boundary condition where set according to table 7.5. Laminar flow is assumed for simplicity.

Table 7.5: Summary of boundary conditions.

Boundaries	Chosen boundary type
Walls	u: No-slip, α, p: zero gradient
Atmosphere	p: standard, α: zero gradient, u: inlet-outlet

7.5 Transport properties

Transport properties, in this case density, viscosity and surface tension are defined in a file called transportProperties. The transport properties used for these simulations are given in table 7.6. All phases are considered to be incompressible, Newtonian fluids.

Table 7.6: Overview of the parameters for the simulation.

Parameter	Symbol	Value	Units
Alumina density	ρ_a	1200	kg/m^3
Alumina kinematic viscosity	ν_a	10^{-6}	m^2/s
Gas density	ρ_g	1.225	kg/m^3
Gas kinematic viscosity	ν_g	$1.461 \cdot 10^{-5}$	m^2/s
Bath density	ρ_b	2000	kg/m^3
Bath kinematic viscosity	ν_b	10^{-6}	m^2/s
Surface tension gas alumina	σ_{ga}	0.03	N/m
Surface tension gas bath	σ_{gb}	0.07	N/m
Surface tension bath alumina	σ_{ba}	0.07	N/m

7.6 Numerical solution

The PIMPLE algorithm was used to solve the pressure velocity coupling. Gradients were solved with cubic scheme, while divergence was solved by applying Fromm's scheme. The time step was set in order to have a Courant-Friedrichs-Lewy (CFL) number less than 0.5.

8. Simulation results

Simulations were run on a small cluster running CentOS 7.4 with 4 Xeon E5-2650 CPUs running at 2.2 GHz equipped with 128 Gb RAM. The computational time of simulations was about 16 hours. Two cases were run, with different drop heights: 2.5 and 5 cm.

Screenshots for the cases are given in figure 8.1 and 8.2. Plots of the bath interface for six different times for the two different cases are shown in figure 8.3 and 8.3. Streamlines and velocity field for the case with drop height at 2.5 cm are shown in figure 8.5 and 8.6, respectively.

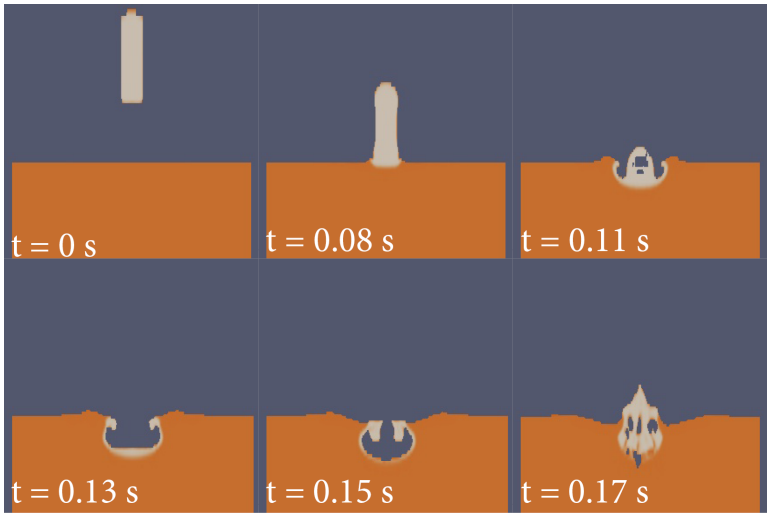

Figure 8.1: Motion of dose of alumina dropped at a height of 2.5 cm at selected times.

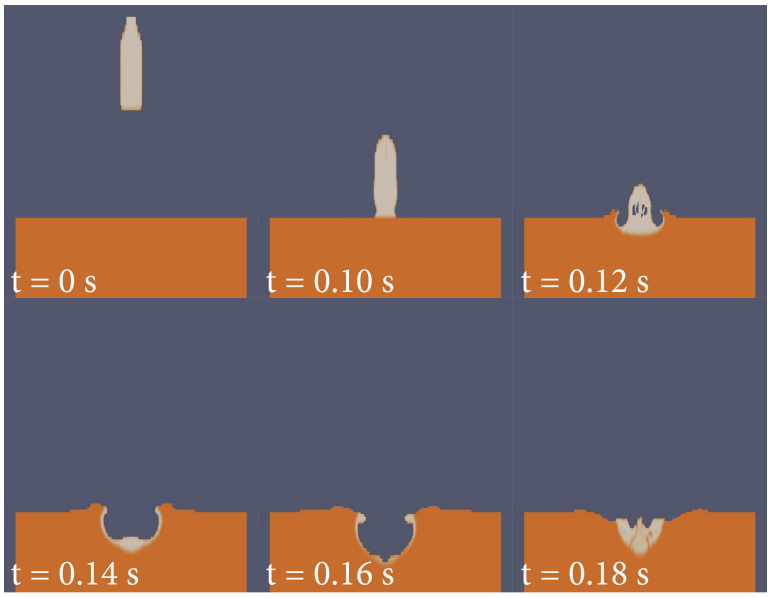

Figure 8.2: Motion of dose of alumina dropped at a height of 5 cm at selected times.

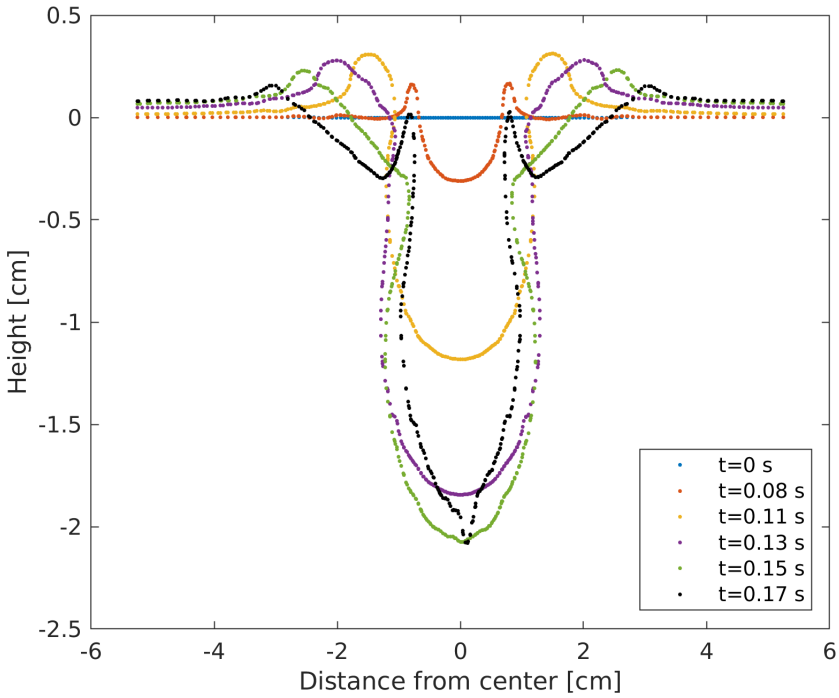

Figure 8.3: Plot of the interface of the bath for the case were drop height is set to be 2.5 cm.

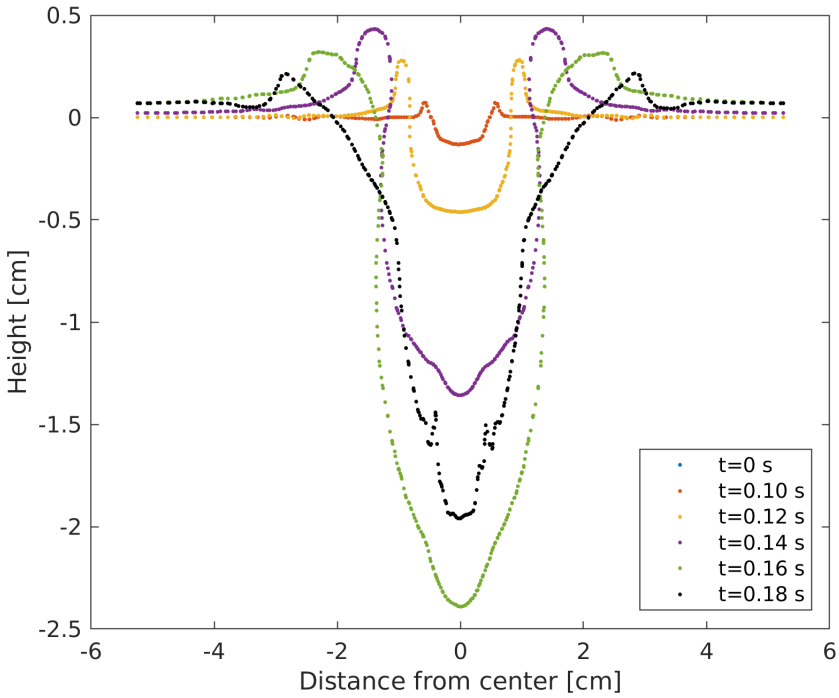

Figure 8.4: Plot of the interface of the bath for the case were drop height is set to be 5 cm.

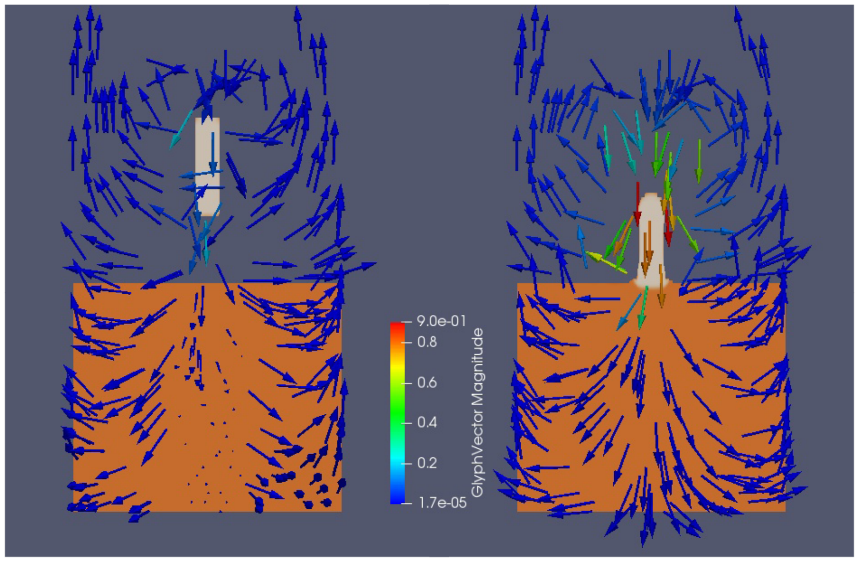

t= 0.01 s t= 0.08 s

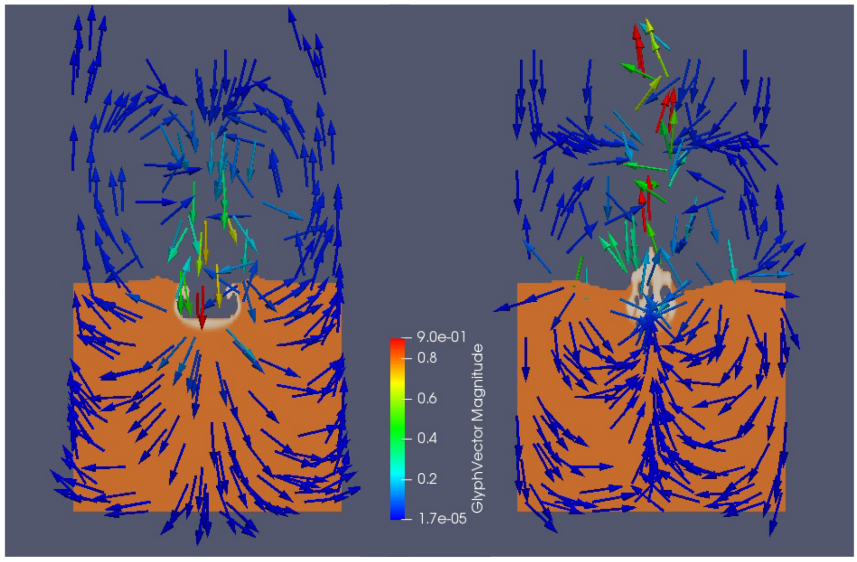

t= 0.13 s t= 0.14 s

Figure 8.5: Velocity field for four selected times, where drop height is 2.5 cm.

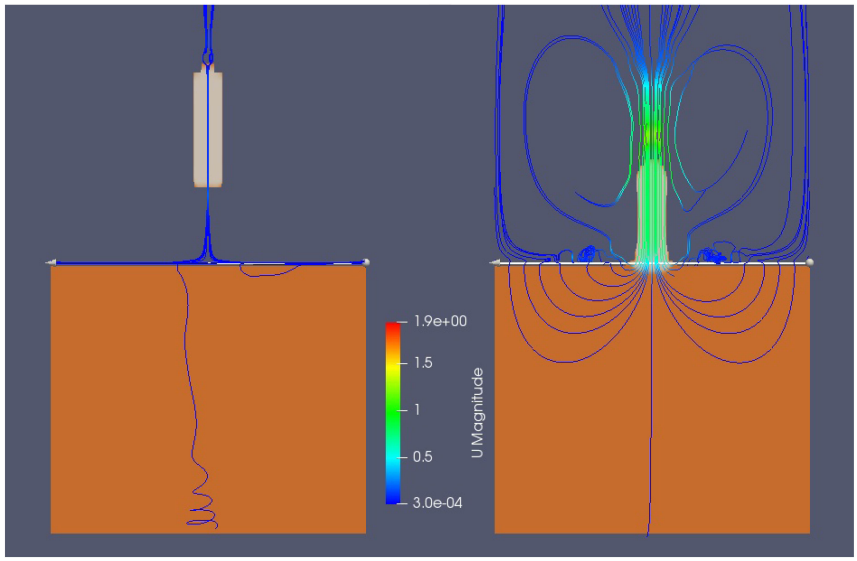

t= 0.01 s t= 0.08 s

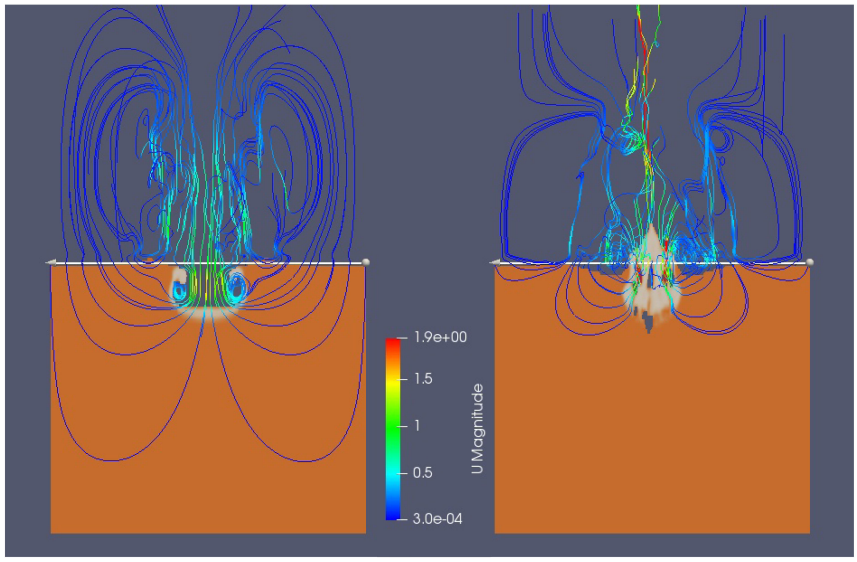

t= 0.13 s t= 0.14 s

Figure 8.6: Velocity field for four selected times, where drop height is 2.5 cm.

9. Discussion

9.1 Mass gain and loss

Laboratory experiments showed a fast mass gain for the rafts fetched. The reason for the mass gain is bath that will freeze around the cold alumina. Some of the alumina will dissolve immediately[21], which means that the mass of bath in the raft is higher than the mass gain illustrated in figure 5.1. At 970 °C, freezing will happen quite rapid, followed by a more slowly melting. The weight loss observed in this experiment is linear, with a dissolution rate within the same scale as found by Yang et al. [43]. Figure 5.3 shows that there is a positive correlation between mass and surface area, which is expected.

Figures 5.1-5.2 shows that there are uncertainties in the measurements, and source of errors should be discussed. One of those is loss of mass upon fetching of rafts. As observations during fetching were impossible, it is uncertain if the whole raft were fetched. Mass might also get lost by melting of bath after removal of raft from the bath, as it will not be cooled down immediately. An estimation of loss by fetching can be done by considering the number of tries were no rafts were fetched, which gives an uncertainty of 14 %.

Another source of error is the removal of rafts from the ladle. Following the extraction of the ladle and removal of the raft, the ladle was on average found to have a an increased mass corresponding to 45 % of the raft. Although a large portion of this mass gain can be credited to bath freezing on the vertical rods of the ladle, it is probable that parts of this mass gain also is due to parts of the raft remaining on the on the ladle. Both are marked in figure 9.1. As the nature of the deposits remaining on the ladle were not investigated further in the scope of this work, this feature introduces an uncertainty in the measurements which, due to its magnitude, is a plausible source to the relatively large variation seen in figures 5.1-5.2. Evidently, reducing the amounts of deposits on the ladle could reduce this error source and solutions to this should be sought for future experiments.

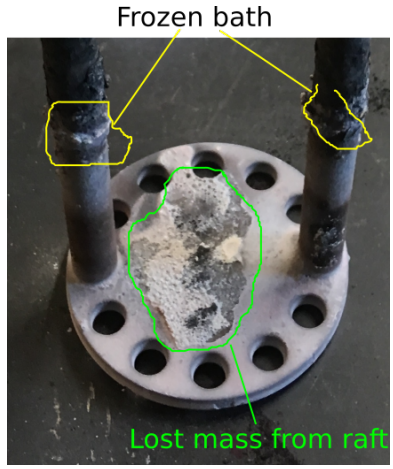

Figure 9.1: Image of a ladle after removal of raft.

The feeding technique could also be a source of error. As the feeding pipe were placed manually each time, the preheating of alumina will vary in order of some few seconds. The alumina will still be cold when hitting the bath surface, and uncertainty due to this can be neglected when comparing with the uncertainty due to fetching and removal.

Further development of this method should be to ensure that the whole sample is collected upon removal of the ladle. This might be solved by having an edge around the ladle, or change it to have shape more equal to a sieve. Having more and smaller holes could also be considered, but these holes might be clogged upon removal.

9.2 Structure

Images show that the structure of the raft varies even for those fetched on the same time. Some rafts contains one or more large spheres in the rafts, many contain one or more craters, while some are all flat. Investigations of cross section revealed that the samples the interior of the spheres (figures 5.5 and 5.7) mainly consisted of one or more large pores. The cold experiments done suggest that this could be due to air that is dragged into the bath together with the powder. As bath will freeze around the raft rapidly, air bubbles with not be able to escape and thus getting trapped in the raft. However, other reasons should also be considered. Humidity in alumina will give release of vaporized water[37] and can also react and form HF-gas[3]. By the data obtained from table 4.2, one can assume a moisture content of 0.5 mass%, i.e. 0.02 g water in a 4 g dose. This will result in 34 mL steam at 100 °C and standard pressure[36], which is much more than needed to form the pores observed in the sample. The pores

will give buoyancy and reduce the bulk density to the raft, and hence increase its flotation time.

It was also revealed that some rafts had frozen bath on the top of the rafts. The powder will penetrate below the bath surface, creating a opportunity for bath to cover the top of the raft. It will still float as the bulk density of the raft will is lower than the density of the bath, as demonstrated by Walker et al. [37]. Bath would also have covered the entire raft if it has sunken before fetching of the ladle. For security reasons, this could not be observed or recorded. Observations are important and the literature review done shows that see-through cells gives opportunities for observing and recording the raft formation.

Very dense layer is seen in the sample containing a crater (figure 5.6). Dense layers are also observed in the the bottom of other samples as well. A crater might be a sphere were the top has melted away. This can happen if hot bath covers over the sphere, which might happens as the powder hits the surface or the raft sinks into the bath.

Light microscope also reveal that rafts consist of several small grains with a diameter around 100 µm. The size and shape of these are similar to the alumina grains observed in figure 5.4. It was not possible too observe any difference in alumina particles at different locations in the raft. SEM should be considered, as this can giver results that can be compared with other research[3].

A layer of pure frozen bath was not found on the bottom of the raft, as alumina grain was observed in these regions. In previous experiments where these layers has been commented[38], alumina was packed together before immersed into the bath. The frozen layer was then melted away after 50 seconds. In the current experiments, alumina powder was able to spread out on the bath surface, which create a thinner layer of alumina that bath can freeze upon. The superheat is also higher than in Walker's experiments, such that the frozen bath layer could have melted away before 30 seconds. The ladle will be as hot as the bath upon removal, which result in that bath still will melt away even after the ladle has been removed from the bath. One can observe a distinct pink layer at the bottom of some of rafts, which is a sintered infiltration layer described in earlier research [38][31]. This indicate that the same mechanism described by Walker [38] will occur, but some layers has already melted away.

Due to a restricted time budget, no more sample could be prepared and viewed in light microscope. It is hard do draw conclusions on how the structure change from the limited amount of sample analyzed. More analysis should be done as further work.

9.3 Effect of changed temperature

Lowering the temperature, and hence the superheat of the bath gave a much higher mass gain, as can be seen in figure 5.1. The liquidus of the bath used is not possible to calculate by the data given (table 4.1), but 945 °C should be close to the liquidus based on the NaF-AlF_3 phase diagram (figure 2.7). It is therefore two cases: one with high superheat, and one where the superheat is low.

The values at 945 °C are way out of the error bar for the measurements at 970 °C, indicating that the process is different as the superheat is low. Reduced superheat seems to give a slower dissolution, which is in accordance with other research[42]. A reason for the deviation might be that at high superheat, mass transfer will dominate the dissolution process[21]. This effect will be even more remarkable as there is no stirring in the bath, which create concentration gradients. The increase in mass gain is due to freezing of more bath, which is heat transfer controlled. A low superheat will let more bath freeze and melting will be slower. This illustrate the effect heat transfer has on the dissolution. More measurements at low superheat should be done, in order to achieve more certain results.

Reduced superheat did not change the surface area of the rafts (figure 5.2), which means that the freezing happens in vertical direction. This is not in accordance with results by Kaszás et al. [16], where increased superheat resulted in a larger spreading, and hence a higher surface area.

More knowledge at lower temperatures (about 950 °C) would also be more similar to conditions found in industrial cells. This methods might be used but was not chosen here for multiple reasons. First of all, the low temperature can give problems as the ladle is immersed into the bath, leading to freezing of bath as the ladle is immersed. However, this can be solved by increasing the power of the furnace while the ladle is immersed down. The second and bigger problem is the fact that the low superheat will result in pure frozen bath will freeze on the ladle, making it hard to distinguish that with what has frozen due to addition of cold alumina. As explained earlier, it is a large source for uncertainties at 970 °C, and it will probably cause even larger uncertainties at lower superheat. This points out the importance of find ways to reduce this source of error.

Cross section image of sample collected at 950 °C shows that there are more pores in this sample than the one fetched at higher temperatures. This is also commented in Kobbeltvedt [18]'s thesis. Why pores occur and the effect bath temperature has on the formation of these has not been investigated yet, and should be looked further into.

9.4 Simulations

Simulations were done in order to investigate whether they can explain observations from laboratory experiments.

As seen in figure 8.1 and 8.2. The penetration will be so deep that bath can cover the surface of the raft formed. This can explain why frozen bath were observed on the top of some of the sample fetched during laboratory experiment. The rafts can still float after being covered with bath, as long as the density is low enough.

From figure 8.5, the batch will hit the bath surface with a velocity around 1 m/s. An increased drop height gave a higher velocity, deeper penetration and the width of the depression formed is thinner (figures 8.3-8.4). This is expected, as the batch will hit the surface with a higher velocity and hence force.

Both figures shows that there air will be trapped in the as the dose hits the bath surface. In real case, bath might have frozen around the particles and trapped some air, which will be seen as pores in samples pulled out.

Streamlines are not symmetric (figure 8.6), due to vortex shedding in the wake of the dose. These effect effects shows also that air are dragged into the bath as the dose hits the bath interface. However, these effect are stronger in turbulent flow, and one should consider a turbulence model instead of assuming laminar flow.

Freezing will have the largest impact on the spreading of the powder. It is not viewed in these simulations, as it is an isothermal model. This is the largest weakness of and biggest source for errors, when comparing to errors due to numerical methods and a coarse mesh.

A 3D model did not give any new effects that were not seen in a 2D-model[11]. When developing this model further, one should consider to use 2D-model, as 2D require lesser computational time.

9.5 Industrial relevance

Observations in industrial cells[11] shows that there will be dry powder on the top of the raft. This is due to the much larger amount (1 kg) of alumina added. By assuming that one feeder is adding 1 kg alumina over a third of center channel[6] (20·300 cm) will result in a distribution of about 0.18 g/cm^2. The same number for the laboratory cell is 0.046 g/cm^2. The dose size is smaller relative to a dose in an industrial cell, and it should be considered to increase the dose size in further work.

Pores are also observed in industrial samples[11] observed will obliviously affect the raft's ability to float. A raft can hinder dissolution, as dry alumina located on the top of raft will not be in contact with the bath. This also points about the importance of finding the origins of pores, as it also affects raft formation in industrial cells.

Observations from industrial cells show that the geometry of the surface area and size of surface area will have an important effect on shape of rafts. This is also commented by Kaszás et al. [16]. The center channel and areas between the anode will have rectangular shape, while the crucible used for experiments is round. This results in rafts with different shape.

In a real cell, there will be convection due to magnetic fields, as well as bubbles from anodic gases. It will lead to splashing of bath, which in an industrial cell will lead to dissolution of rafts from the sides[11]. This will also result in a faster dissolution rate than the one observed in this experiment. These effects can also be considered in a laboratory cell by having a stirrer and purge gas into the bath.

10. Concluding remarks

In the present work, formation and dissolution of rafts were investigated. A cold model with alumina and water was created in order to predict what will happen in a laboratory furnace. One could observe that alumina will capture air as it is fed down to the cell. A cold model could be even better if the rapid freezing as alumina hits the bath is considered.

Alumina rafts were created and fetched in a laboratory furnace. Rafts were fetched at a temperature of 970 °C, in a time interval between 30 and 300 seconds. An important objective is to create a reproducible method at a lab cell, where single parameters are easier to control. At the given condition, rafts formed fast, and dissolved at a constant rate of 0.8 g/min.

Mass loss when fetching the raft, and loss of mass during removal of raft were found to be the largest sources of error. Creating an edge on the ladle might help in order to avoid mass loss during fetching. Bath that freeze due to removal contribute to uncertainty in the mass of the raft, which is an uncertainty that is hard to reduce.

The rafts fetched varied in structure. Most of the rafts had craters or a sphere on their surface. Investigation in light microscopy revealed that the sphere contained large amounts of pores. This could be do to air that is captured by the dose as it hits the bath surface. Bath will freeze around immediately such that the air cannot escape. Calculation showed that the alumina fed contains enough moisture that vaporized water and evolution of HF-gas also can also create pores in the raft. The pores will give buoyancy, and might hinder dissolution in electrolysis cells. More investigations should be done in order identify origin of the pores and how porosity of a raft affect its dissolution.

The rafts did not contain a layer of frozen bath, but a distinct pink layer was observed in the bottom of multiple samples, which indicate the same infiltration mechanisms as described in earlier research.

Reducing the temperature to a value close to the liquidus of the melt will gave a higher mass gain and a slower dissolution. The lower superheat resulted in more freezing of bath, thus increasing mass gain. This illustrate the effect heat transfer has on the dissolution process. Most smelter operate at low superheat. Further experiments should therefore be done at lower superheat in order to have better industrial relevance.

Experiment will also be more industrial relevant by applying convection and bubbles. A larger dose of alumina should also be considered.

Simulation of alumina being fed to cryoilte with conditions equal to the experimental one was done, assuming all phases to be Newtonian fluids and isothermal conditions. The simulations demonstrate interactions that happens as alumina hits the bath surface, for example immersion of bath as the particle hits the surface. The simulations also show that a dose will drag air into the bath as it hits the surface. This will give an explanation of the pores observed. However, this model does not consider the rapid freezing of bath and heat transfer, as it is an isothermal model. Further development should be on applying the heat equation, such that freezing and melting of bath can be simulated. By comparison of earlier work, a 3D-model gives quite similar result than a 2D-model. Further development can therefore be done in a 2D-model, which reduce the amount of computational time needed.

Both experiments and simulations are good ways to obtain a better knowledge of the alumina dissolution. Findings can result in new technology that can be implemented in industrial cells, resulting in a more efficient feeding, lesser emissions and better energy efficiency of the Hall–Héroult process.

List of notation

Sub- and superscripts

d : Dissolved specie
$_e$: East face
$_E$: East node
$_f$: Arbitrary face
g : Gaseous phase
$_{i,j}$: Indices for direction
k : Arbitrary phase
l : Liquid phase
$_n$: North face
$_N$: North node
NI : Number of cells in x-direction
NJ : Number of cells in y-direction
$_P$: Central node
$_s$: South face
$_S$: South node
s : Solid phase
$_w$: West face
$_W$: West node

Symbols

$\boldsymbol{a}$	: Acceleration vector	[m/s^2]
A	: Area	[m^2]
α	: Phase fraction	[]
ϵ	: Tolerance value	[]
CS	: Control surface	[m^2]
CV	: Control volume	[m^3]
dA	: Infinitesimal surface area	[m^2]
dS	: Infinitesimal surface element	[m^2]
dV	: Infinitesimal volume element	[m^3]
δ	: Contact angle	[]
η_{Al}	: Stoichiometric constant for aluminum	[]
η_e	: Stoichiometric constant for electrons	[]
$\boldsymbol{f}$	: Body force per unit mass	[N/(m^3 kg)]
$\mathscr{F}$	: Faraday's constant	[C/mol]
$\boldsymbol{F}_i$	: Forces acting on a body	[N]
F_b	: Buoyancy force	[N]
F_g	: Gravitational force	[N]
F_s	: Force due to surface tensions	[N]
$\boldsymbol{F}^b$	: Body force	[N]
$\boldsymbol{F}^s$	: Surface force	[N]
g	: Gravitational acceleration	[m/s^2]
γ	: Surface tension	[N/m]
Γ	: General diffusion parameter	[various]
h_0	: Drop height	[m]
l	: Triple line	[m]
λ	: Relative tolerance value	[]
m	: Mass	[kg]
$\dot{\boldsymbol{m}}$	: Mass flux	[kg/(s m^2)]
$\boldsymbol{M}$	: Momentum source due internal interactions	[N/m^3]
M_{Al}	: Molar mass of aluminum	[kg/mol]
$\boldsymbol{n}$	: Surface normal vector	[1/m]
μ	: Molecular viscosity	[kg/(m s)]
n	: Number of iterations	[]
ν	: Kinematic viscosity	[m^2/s]
p	: Pressure	[N/m^2]

I	: Cell current	[A]
i_{Al}	: Current density used to form aluminum	[A/m^2]
i_l	: Current density loss	[A/m^2]
ϕ	: General scalar property	[various]
R	: Cell resistance	[Ohm]
$\dot{R}$	: Reaction rate per volume	[kg/(s m^3)]
ρ	: Mass density	[kg/m^3]
ρ_l	: Mass density of liquid	[kg/m^3]
ρ_p	: Mass density of particle	[kg/m^3]
S_ϕ	: General source term	[various]
S_u	: Linearised source term	[various]
σ	: Surface tension	[N/m]
t	: Time	[s]
$\boldsymbol{T}$	: Stress tensor	[N/m^2]
$\boldsymbol{\tau}$	: Viscous shear stresses	[N/m^2]
$\boldsymbol{u}$	: Velocity vector	[m/s]
u, v	: Velocity components in x- and y-directions	[m/s]
$\boldsymbol{v}$	: Velocity where mass transfer occurs	[m/s]
U	: Cell voltage	[V]
V	: Volume	[m^3]
V_i	: Immersed volume of a particle	[m^3]
V_p	: Volume of a particle	[m^3]
W_{el}	: Specific energy consumption	[kWh/kg]
x_{Al}	: Current efficiency with respect to aluminum	[]
x, y, z	: Coordinates	[m]

Acronymes

B.E. T : Braunauer, Emmet and Teller
CFD : Computational fluid dynamics
CFL : Courant-Friedrichs-Lewy
CT : Computed Tomography
SEM : Scanning Electron Microscopy
SGA : Smelter Grade Alumina
VOF : Volume of Fluid
XRD : X-ray diffraction

Bibliography

[1] Atkins, P. and Paula, J. d. P. (2014). *Physical Chemistry*. Oxford university press, Oxford, 10 edition.

[2] Barton, I. E. (1998). Comparison of SIMPLE- and PISO-type algorithms for transient flows. *International Journal for Numerical Methods in Fluids*, 26(4):459–483.

[3] Dando, N., Wang, X., Sorensen, J., and Xu, W. (2010). Impact of thermal pretreatment on alumina dissolution rate and HF evolution. In Johnson, J. A., editor, *Light Metals 2010*, pages 541–546. TMS, Warrendale, Pa.

[4] Dassylva-Raymond, V., Kiss, L. I., Poncsak, S., Chartrand, P., Bilodeau, J.-F., and Guérard, S. (2014). Modeling the behavior of alumina agglomerate in the Hall-Héroult process. In Grandfield, J., editor, *Light Metals 2014*, pages 603–608. Wiley, Hoboken,.

[5] Einarsrud, K. E. (2008). The effect of detaching bubbles on aluminium-cryolite interfaces. Master's thesis, Norwegian University of Science an Technology, Trondheim.

[6] Einarsrud, K. E. (2012). *A treatise on interpolar transport phenomena*. Phd thesis, Norwegian University of Science and Technology, Faculty of Engineering Science & Technology, Department of Energy and Process Engineering, Trondheim.

[7] Einarsrud, K. E., Gylver, S. E., and Manger, E. (2018). CFD Modelling of Alumina Feeding. In Martin, O., editor, *Light Metals 2018*, pages 557–564. Springer International Publishing, Cham.

[8] Çengel, Y. A. and Cimbala, J. M. (2014). *Fluid mechanics : fundamentals and applications*. McGraw-Hill, Boston, 3rd ed. in si units. edition.

[9] Greenshields, C. (2017). OpenFOAM v5 User Guide: 5.3 Mesh generation - blockMesh. https://cfd.direct/openfoam/user-guide/blockmesh/. Retrived 2018-05-10.

[10] Grotheim, K. and Kvande, H., editors (1993). *Introduction to Aluminium Electrolysis-Understanding the Hall-Heroult Process*. Aluminium-Verlag, Düsseldorf.

[11] Gylver, S. E. (2017). *Alumina dissolution in cryolite: an investigation of raft formation*. Project report, Norwegian University of Science an Technology, Trondheim.

[12] Haverkamp, R. G. and Welch, B. J. (1998). Modelling the dissolution of alumina powder in cryolite. *Chemical Engineering and Processing: Process Intensification*, 37(2):177–187.

[13] Hirt, C. W. and Nichols, B. D. (1981). Volume of fluid (VOF) method for the dynamics of free boundaries. *Journal of Computational Physics*, 39(1):201–225.

[14] Hudson, L. (1987). Alumina production. In Burkin, A., editor, *Production of Aluminium and Alumina*, volume 20 of *Critcal Reports on Applied Chemistry*, pages 11–46. John Wiley & Sons, Chichester.

[15] Kaszás, C., Kiss, L., Guérard, S., and Bilodeau, J.-F. (2015). Behavior of Powders on the Surface of a Liquid. In Hyland, M., editor, *Light Metals 2015*, pages 639–642. Springer, Cham.

[16] Kaszás, C., Kiss, L., Poncsák, S., Guérard, S., and Bilodeau, J.-F. (2017a). Spreading of Alumina and Raft Formation on the Surface of Cryolitic Bath. In Ratvik, A. P., editor, *Light Metals 2017*, The Minerals, Metals & Materials Series, pages 473–478. Springer, Cham.

[17] Kaszás, C., Kiss, L. I., Poncsák, S., Bilodeau, J.-F., and Guérard, S. (2017b). Flotation and Infiltration of Artificial Rafts on the Surface of Molten Cryolite. In *34th International Conference and Exhibition of ICSOBA*, Quebec.

[18] Kobbeltvedt, O. (1997). *Dissolution kinetics for alumina in cryolite melts : distribution of alumina in the electrolyte of industrial aluminium cells*. Phd thesis, Norwegian University of Science and Technology, Department of Electrochemistry, Trondheim.

[19] Kobbeltvedt, O., Thonstad, J., and Rolseth, S. (1996). On the mechanisms of alumina dissolution with relevance to point feeding aluminium cells. In Hale, W., editor, *Light Metals 1996*. TMS, Warrendale, Pa.

[20] Kreyszig, E. (2011). *Advanced engineering mathematics*. Wiley, Hoboken, N.J, 10th ed., international student version. edition.

[21] Lavoie, P., Taylor, M. P., and Metson, J. B. (2016). A Review of Alumina Feeding and Dissolution Factors in Aluminum Reduction Cells. *Metallurgical and Materials Transactions B*, 47(4):2690–2696.

[22] Liu, X., George, S. F., and Wills, V. A. (1994). Visualisation of alumina dissolution in cryolitic melts. In Mannweiler, U., editor, *Light Metals 1994*, pages 359–359. TMS.

[23] OpenCFD (2017). Solution and algorithm control. https://cfd.direct/openfoam/user-guide/fvsolution/.

[24] OpenCFD (2018a). multiphaseinterfoam.c File Reference. https://www.openfoam.com/documentation/cpp-guide/html/multiphaseInterFoam_8C.html.

[25] OpenCFD (2018b). OpenFOAM® - Official home of The Open Source Computational Fluid Dynamics (CFD) Toolbox. http://www.openfoam.com.

[26] Pedersen, B. (2017). Aluminium. http://snl.no/aluminium. From Store Norske Leksikon.

[27] Picard, D., Tessier, J., Gauvin, G., Ziegler, D., Alamdari, H., and Fafard, M. (2017). Investigation of the Frozen Bath Layer under Cold Anodes. *Metals*, 7(9):374.

[28] Richerson, D. W. (2005). *Modern ceramic engineering: properties, processing, and use in design*. CRC press.

[29] Rolseth, S. and Thonstad, J. (1991). Agglomeration and dissolution of alumina in cryolite baths. In Sahoo, M. and Pinfold, P., editors, *Extraction, Refining, and Fabrication of Light Metals*, Proceedings of Metallurgical Society of Canadian Institute of Mining and Metallurgy, pages 177–190, Amsterdam. Pergamon.

[30] Simonsen, A. J., Einarsrud, K. E., and Eick, I. (2015). The Impact of Bubble-Bubble Interaction on Anodic Gas Release: A Water Model Analysis. In *Light Metals 2015*, pages 795–800. Springer, Cham.

[31] Østbø, N. P. (2002). *Evolution of alpha phase alumina in agglomerates upon addition to cryolitic melts*. Phd thesis, Norwegian University of Science an Technology - NTNU, Trondheim.

[32] Thonstad, J., Fellner, P., Haarberg, G. M., Híveš, J., Kvande, H., and Sterten, . (2001). *Aluminium Electrolysis: Fundamentals of the Hall-Héroult Process. 3rd*. Aluminium-Verlag, Düsseldorf.

[33] Thonstad, J., Nordmo, F., and Paulsen, J. B. (1972). Dissolution of alumina in molten cryolite. *MT*, 3(2):407–412.

[34] Townsend, D. W. and Boxall, L. G. (1984). Crusting behavior of smelter aluminas. In McGeer, J. P., editor, *Light Metals 1984*, pages 613–621. TMS.

[35] Versteeg, H. K. and Malalasekera, W. (2007). *An introduction to computational fluid dynamics: the finite volume method*. Pearson/Prentice Hall, Harlow, 2nd ed. edition.

[36] Wagner, W. (2008). *International Steam Tables : Properties of Water and Steam Based on the Industrial Formulation IAPWS-IF97*. Springer Berlin Heidelberg, 2nd ed. edition.

[37] Walker, D., Utigard, T., Toguri, J., and Taylor, M. (1992). Behaviour of Alumina Powder Agglomerates Upon Addition to Cryolite-Based Electrolytes. In *Advances in Production and Fabrication of Light Metals and Metal Matrix Composites;*, pages 23–37, Edmonton, Alberta, Canada.

[38] Walker, D. I. (1993). *Alumina in aluminum smelting and its behaviour after addition to cryolite-based electrolytes*. Phd thesis, Univeristy of Toronto, Toronto.

[39] Walker, D. I., Utigard, T., and Taylor, M. P. (1995). Alumina agglomerates in aluminum smelters. In Evans, J. W., editor, *Light Metals 1995*, pages 425–434. TMS.

[40] Welch, B. J. and Kuschel, G. I. (2007). Crust and alumina powder dissolution in aluminum smelting electrolytes. *Journal of Metals*, 59(5):50.

[41] Whittington, B. and Ilievski, D. (2004). Determination of the gibbsite dehydration reaction pathway at conditions relevant to Bayer refineries. *Chemical Engineering Journal*, 98(1):89–97.

[42] Yang, Y., Gao, B., Wang, Z., Shi, Z., and Hu, X. (2015a). Effect of Physiochemical Properties and Bath Chemistry on Alumina Dissolution Rate in Cryolite Electrolyte. *JOM*, 67(5):973–983.

[43] Yang, Y., Gao, B., Wang, Z., Shi, Z., and Hu, X. (2015b). The Formation and Dissolution of Crust Upon Alumina Addition into Cryolite Electrolyte. *Journal of Metals*, 67(9):2170–2180.

[44] Yang, Y., Gao, B., Wang, Z., Shi, Z., and Hu, X. (2015c). Study on the Dissolution of Alumina in Cryolite Electrolyte Using the See-Through Cell. In Hyland, M., editor, *Light Metals 2015*, pages 583–588. Springer, Cham.

[45] Zhan, S.-q., Li, M., Zhou, J.-m., Yang, J.-h., and Zhou, Y.-w. (2015). Analysis and modeling of alumina dissolution based on heat and mass transfer. *Transactions of Nonferrous Metals Society of China*, 25(5):1648–1656.